Soft Matter

PAPER

View Article Online
View Journal | View Issue

Cite this: *Soft Matter*, 2025, **21**, 8569

Magnetocolloidal impulses as stealth mixers to curb scalar Taylor dispersion in microfluidics

Zakaria Larbi,[a] Faïçal Larachi,*[a] Seyed Mohammad Taghavi[a] and Abdelwahid Azzi[b]

Scalar mixing in microfluidics is often limited by the dominance of laminar flow and weak transverse transport, which restrict effective mixing despite the enhanced axial spreading provided by Taylor–Aris dispersion. Here, we demonstrate that injecting pulses of magnetic nanoparticles (MNPs) in conjunction with static or rotating magnetic fields can actively reshape scalar dispersion dynamics. Static fields drive Kelvin body forces (KBF) at pulse fronts, while rotating fields superimpose torque-induced spin-up flows that enhance cross-stream transport and improve scalar mixing compared to no-field injection. At high MNP Péclet numbers (Pe $\approx 10^4$) and short residence times, the interplay between KBF and spin-up dynamics yields concentration front oscillations and partial detachment, indicative of three-dimensional secondary flows. For longer residence times, sustained spin-up flow ensures efficient cross-stream homogenization, with the MNP variance reduced by nearly 85% relative to the no-field case, while the scalar variance decreases by about 70%. These results demonstrate that magnetically actuated colloidal impulses, through controlled MNP pulse injection under rotating magnetic field action, can generate three-dimensional secondary structures and establish a new strategy for high-efficiency mixing in microfluidic systems.

Received 25th August 2025,
Accepted 14th October 2025

DOI: 10.1039/d5sm00861a

rsc.li/soft-matter-journal

1 Introduction

Microfluidics has emerged as a transformative revolution in chemical and biological engineering, enabling unprecedented manipulation of minute fluid volumes within miniature channels.[1–3] Scaling down to such dimensions has opened new application niches beyond traditional large-scale reaction and separation unit operations, where the daunting challenges of scale-up can often be addressed through straightforward numbering-up strategies.[4] These advances stem from a set of intrinsic advantages: (i) the use of small fluid volumes enables precise control of operating conditions, thereby mitigating hazards[5,6] and fostering reproducibility;[7–9] (ii) taming the hosting geometry into much shorter characteristic microchannel lengths unleashes molecular diffusion at its full potential;[10] and (iii) the consequentially high surface-to-volume ratio ensures efficient heat and mass transfer for fast reactions and/or high thermicity.[5,6,11] Together, these features have made microfluidics fertile ground for applications in chemical synthesis, diagnostics,[12–14] lab-on-a-chip devices,[15,16] and biomedical analysis.[3,17,18]

However, microfluidic systems present a major challenge: the flows in such systems are laminar.[19,20] This is due to the small characteristic dimensions of the channels, which lead to very low Reynolds numbers (Re < 1).[21] In this regime, inertial effects are negligible, and thus no convective instabilities or turbulence can arise to enhance mixing. Consequently, molecular diffusion remains the sole mixing mechanism. Yet, in microfluidics, advection dominates over diffusion, since the residence time of the fluid cannot be reduced to values comparable to the long characteristic diffusion times.[22,23] The transport regime is therefore governed by the Péclet number (Pe), which represents the ratio of advective to diffusive transport. In most microfluidic applications, Pe $\gg 1$, implying that diffusion alone is insufficient to achieve efficient mixing.[22,23]

To overcome this limitation, additional mixing strategies are required to enhance mixedness rates in microfluidic reactors. Broadly, two approaches have been developed. The first, known as passive mixing, relies on micropatterned channels or geometrical structures to induce chaotic advection and improve fluid interpenetration.[19,22,23] For instance, Javed *et al.*[23] performed a mathematical analysis of three passive micromixer geometries—namely, a simple T-junction, a spiral T, and a three-dimensional serpentine mixer (TDSPM). Their results showed that the TDSPM, characterized by repeated U-shaped

[a] *Department of Chemical Engineering, Université Laval, Québec, QC G1V 0A6, Canada. E-mail: faical.larachi@gch.ulaval.ca*
[b] *Laboratoire de Transports Polyphasiques et Milieux Poreux, Faculté de Génie Mécanique et Génie des Procédés, Université des Sciences et de la Technologie Houari Boumédiène, BP 32, El Alia, Bab Ezzouar, 16111 Algiers, Algeria*

bends and a rectangular inlet, significantly enhances fluid interaction and achieves markedly higher mixing efficiency than the other designs. The second strategy, termed active mixing, exploits external force fields to perturb parallel streamlines and promote transversal transport. Various physical mechanisms have been proposed, including electrophoresis, acoustic forcing,[20,24,25] and magnetic actuation.[26–28] As an illustration, Mehta and Mondal[25] investigated the flow of viscoplastic fluids through a microchannel containing a bipartite cylinder whose surfaces carry electrical potentials of identical polarity but differing magnitudes. Their study revealed that electroosmotic forcing, arising from geometry-modulated electrical double-layer effects, interacts with viscous stresses to induce local flow reversal near the obstacle. This mechanism generates recirculating vortices both upstream and downstream of the channel, leading to complex swirling structures that substantially enhance mixing beyond what diffusion alone could achieve.

One popular strategy for active mixing in microfluidic devices is the use of magnetic colloidal suspensions stimulated by external fields.[29] In such systems, magnetic nanoparticles (MNPs) can be remotely manipulated, a feature that has been increasingly exploited to enhance mixing in microfluidic flows.[28,30,31] A particularly effective strategy relies on the use of rotating magnetic fields (RMFs).[28] Under such excitation, MNPs experience a magnetic torque that is transferred to the carrier liquid, generating a secondary flow commonly referred to as the spin-up flow.[32] This rotational motion counteracts the longitudinal concentration gradients created by laminar advection and significantly enhances transversal mixing. For example, Boroun and Larachi[28] demonstrated that applying an RMF in a T-microreactor performing the Dushman–Villermaux reaction improved micromixing times and reaction selectivity. More recently, Larbi *et al.*[33] investigated the effect of spin-up flow on Taylor dispersion of a passive scalar. Their results highlighted that spin-up flow can effectively suppress the concentration gradients induced by Poiseuille flow, provided that the spin-up velocity exceeds the axial flow velocity, thereby ensuring efficient homogenization. In addition to torque-driven mechanisms, mixing may also be enhanced through Kelvin body force (KBF) effects, which arise when concentration gradients of MNPs are established under a magnetic field. These gradients generate asymmetric pressure distributions that drive convective secondary flows. Larbi *et al.*[34] explored this phenomenon in a Y-shaped micromixer subjected to an RMF. They found that when MNPs were symmetrically injected from both inlets, mixing was solely governed by spin-up flow. However, unilateral injection of nanoparticles produced strong transverse concentration gradients due to the high Péclet number, thereby activating KBF-driven convection. This additional mechanism acted to restore suspension concentration equilibrium by reducing concentration inhomogeneities, thus complementing torque-induced spin-up flow and providing a second pathway for mixing enhancement.

The studies on the effect of MNPs on mixing have been conducted on the basis of the model developed by Larbi *et al.*[35] This model was initially formulated in the general framework of colloidal magnetic suspensions and subsequently adapted to describe spin-up flows. Its validity was assessed against the experimental results of Torres-Diaz *et al.*[36] in the clusterless regime, where nanoparticles are sufficiently diluted to prevent dipole–dipole interactions from forming clusters. The model relies on a two-phase hydrodynamic approach that separates the dynamics of the non-magnetic carrier liquid from those of the MNPs. The mathematical closure was established through Faxén's laws, which describe the torque, drag, and stresslet forces governing liquid–particle interactions. In addition, the transport of nanoparticles and the orientation dynamics of their magnetic moments were described by the Smoluchowski probability density equation, formulated in the case of single nanoparticles consistent with the clusterless assumption.

Research on the use of MNPs in microfluidics has largely focused on two mechanisms: spin-up flow, driven by the magnetic torque under RMFs,[31,33] and KBF, arising from concentration gradients of MNPs.[34] In these studies, secondary flows are mostly confined to the transverse direction, while the axial velocity profile remains essentially unchanged.[33,34] This behavior stems from the Stokesian nature of the flow, where inertial interactions are negligible and axial and transverse effects simply superimpose. Moreover, most prior works employed continuous MNP injection, which limits the formation of strong concentration gradients, particularly along the axial direction. For instance, Larbi *et al.*[34] showed that KBF-driven mixing occurs only over the initial portion of the channel and quickly decays once the gradients are smoothed out, restricting the action of this mechanism to a narrow region. This raises an open question: how does spin-up flow interact with extended concentration gradients, particularly along the axial direction? Properly structured gradients could couple with RMF-induced torque to create three-dimensional secondary flows and enhance mixing, yet prior work considered mostly transverse gradients.

In contrast to this body of work, the key to generating such gradients lies in the pulsed injection of MNPs, which, when combined with RMF excitation, couples with the magnetic torque and KBF to drive both axial and transverse flows simultaneously. This approach inherently produces strong axial concentration variations, resulting in genuinely 3D flow structures and opening new possibilities for micromixing applications. Fundamentally, the problem shifts from the classical framework of Taylor dispersion with passive tracers to the study of dispersion in actively driven magnetic suspensions. To the best of our knowledge, no previous work, since the seminal work of Taylor[37] up to more recent developments on this subject,[38,39] has yet addressed Taylor dispersion in suspensions actively driven by external magnetic fields. Establishing this connection provides not only a robust theoretical foundation but also opens promising avenues for the design of next-generation magnetic micromixers and microreactors operating in a so-called evanescent or 'stealth' mode.

The objective of this study is to analyze the transient transport of MNP pulses in Taylor microcapillary flows under

externally applied magnetic fields. We first aim to characterize the hydrodynamic response induced by a static magnetic field (SMF), focusing on the activation of KBF. We then investigate the influence of an RMF on dispersion dynamics, with particular attention to the role of concentration gradients generated by pulsed injection and to the dependence on the Péclet number for MNP transport. Finally, we extend the framework to the simultaneous injection of MNPs and a passive scalar in order to assess the efficiency of this strategy in enhancing scalar pulse mixing. Ultimately, this work seeks to establish the "MNP pulse + RMF" approach as a versatile pathway for active control of Taylor dispersion and as a foundation for the design of magnetic micromixers and microreactors.

2 Theoretical background

2.1 Hydrodynamic setting for Taylor dispersion with MNPs

This study investigates a dispersion problem in a cylindrical microchannel, inspired by the classical Taylor dispersion phenomenon,[37,38] but adapted to the case of magnetic nanoparticle (MNP) transport. The system consists of a microtube with a radius of $R = 100$ μm and a length of $L = 100 \times R$, within which a laminar Poiseuille flow is established under a constant pressure gradient, as illustrated in Fig. 1. The Reynolds number is very small, $\mathrm{Re} < 1$, ensuring that inertia can be neglected and that the flow remains in the Stokes regime.

At the channel inlet, a short pulse of MNPs is injected as a thin differential disk at $z = 0$, superimposed on the background carrier flow. The nanoparticles are transported downstream by convection and diffusion, while interacting with externally applied magnetic fields. No-slip conditions are imposed on the velocity at the channel walls, and zero-flux boundary conditions are assumed for both MNP and scalar concentrations.

Two types of magnetic fields are considered. The first is an SMF, a time-independent radial field defined as $\vec{H} = H_0\vec{e}_r$, where H_0 is the constant magnitude. The second is an RMF, a time-harmonic field rotating around the longitudinal axis z of the tube at a frequency f_0, expressed in Cartesian coordinates as:

$$\vec{H}(t) = H_0[\cos(2\pi f_0 t)\vec{e}_x + \sin(2\pi f_0 t)\vec{e}_y]. \quad (1)$$

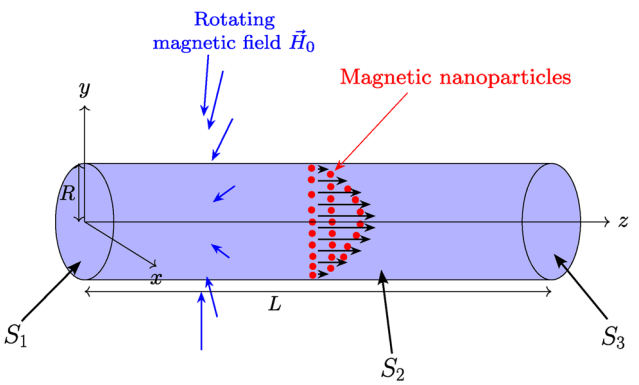

Fig. 1 Schematic description of the microchannel geometry, the imposed pressure-driven Poiseuille flow, and the externally applied magnetic fields (SMF and RMF).

These configurations give rise to two distinct magneto-hydrodynamic mechanisms. Under SMF, the concentration gradients of MNPs activate the Kelvin body force (KBF),[34] which generates transverse and axial flow perturbations. Under RMF, the time-dependent field additionally exerts a magnetic torque on the nanoparticles, leading to a secondary spin-up flow.[33] Together, these mechanisms act on classical Taylor dispersion, modifying the spreading of both the MNP pulse and a co-injected passive scalar.

2.2 Theoretical framework for magnetically driven dispersion

The mathematical formulation of the problem describes the coupled transport of linear momentum in the Newtonian fluid and the dynamics of the MNPs. Due to the microscale dimensions of the tube, the fluid flow is governed by the Stokes equations. An impulse of MNPs is introduced at the inlet and is advected along the axial direction of the tube. The MNP concentration evolves under the combined effects of advection by the fluid and diffusion. Simultaneously, a magnetic field is applied at the lateral boundary of the tube, interacting with the MNPs. This field not only affects the distribution of nanoparticles but also tends to align their magnetic moments, thereby influencing their dispersion behavior. The applied field generates local fluid motion through two mechanisms: the KBF, associated with field gradients, and the magnetic torque, associated with the alignment of MNP magnetic moments. Both act as body forces on the fluid, enhancing transverse flow and perturbing the velocity field. The resulting model therefore couples the background hydrodynamic flow with the advective–diffusive transport of MNPs and their magnetic interactions. The hydrodynamic model of colloidal suspensions employed in this work was originally developed by Larbi *et al.*[35] in the context of spin-up flows. In this framework, a two-phase approach is adopted, separating the contributions of the carrier liquid (non-magnetic) and the dispersed MNPs. The mathematical closure of the model is achieved in the magnetically dilute or clusterless regime by combining Faxén's laws, which describe the hydrodynamic interactions and the exchange of linear momentum between the liquid and the nanoparticles, with the Smoluchowski equation, which governs both the translational transport of the MNPs and the orientational dynamics of their magnetic moments. To ensure the validity of the Smoluchowski description, we deliberately restrict our analysis to dilute suspensions, where dipole–dipole interactions are negligible and no particle aggregation or chain formation occurs under the applied magnetic field.

Considering a creeping flow regime, appropriate due to the small diameter of the tube, the linear momentum equation for the magnetically laden liquid, accounting for the volumetric contributions of the KBF and magnetic torque, is given by:

$$-\vec{\nabla}P + \mu_e\nabla^2\vec{v} + \frac{K_B T}{V_p}\alpha\vec{\nabla}\times\left(\vec{m}\times\vec{H}\right) + \frac{K_B T}{V_p}\alpha\vec{m}\cdot\vec{\nabla}\otimes\vec{H} = \vec{0} \quad (2)$$

Here, $\vec{v}$ is the liquid velocity field and P is the pressure. The effective dynamic viscosity is given by Einstein's relationship, $\mu_e = \mu\left(1+\frac{5}{2}\phi\right)$, where μ is the viscosity of the carrier liquid and ϕ is the local volume fraction of MNPs. The terms involving the Boltzmann constant K_B, absolute temperature T, and particle volume V_p arise from the statistical description of nanoparticle magnetization. The dimensionless magnetic field is defined as $\vec{\tilde{H}} = \vec{H}\big/H_0$, normalizing the applied field by its magnitude. This scaling emphasizes the role of the Langevin parameter α, which quantifies the ratio between magnetic and thermal energies. Finally, $\vec{m}$ represents the average orientation of the MNP magnetic moments. The third term on the left-hand side of eqn (2) represents the torque-induced body force, while the fourth term corresponds to the KBF.

The momentum equation adopted in this work, eqn (2), originates from the two-phase framework developed in ref. 35. In this formulation, separate linear momentum balances are written for the carrier liquid and for the dispersed MNPs. The liquid-phase equation does not contain magnetic body forces since the fluid is non-magnetic, whereas the particle-phase equation includes the magnetic contributions arising from both the magnetic torque and the Kelvin body force. The two balances are coupled through interphase momentum exchange terms modeled by Faxén's law, which ensures the conservation of linear momentum. This coupling is two-way, as the fluid motion influences the particles and the particles, in turn, feed back on the fluid through the exchange terms. The equation of motion presented here, eqn (2), is thus the effective form obtained after combining the two phase-averaged equations and eliminating the interfacial surface-exchange terms, leading to a single macroscopic momentum equation for the colloidal suspension that includes both the liquid and particle contributions. This unified formulation guarantees the conservation of total linear momentum of the suspension and provides a consistent continuum description of the magnetically driven flow. As discussed in our follow-up work,[34] in the dilute limit ($\phi \to 0$), both the magnetic torque and the Kelvin-related contributions vanish, and eqn (2) naturally reduces to the standard momentum equation of a non-magnetic liquid.

At the wall, S_2, eqn (2) is subject to a no-slip boundary condition:

$$\vec{v}_1|_{S_2} = \vec{0} \tag{3}$$

At the inlet S_1, a fully developed Poiseuille flow is imposed with a parabolic velocity profile:

$$\vec{v}_1 \cdot \vec{n}_1|_{S_1} = 2v_0\left(1-\frac{x^2+y^2}{R^2}\right) \tag{4}$$

where v_0 denotes the average inlet velocity, and R is the radius of the tube.

At the outlet S_3, a constant pressure condition is enforced:

$$P|_{S_3} = P_0 \tag{5}$$

The momentum eqn (2) is coupled with the incompressibility condition for the liquid:

$$\vec{\nabla}\cdot\vec{v} = 0 \tag{6}$$

The body forces in the linear momentum eqn (2) depend on the induced magnetic field $\vec{\tilde{H}}$, the orientation of the MNP magnetic moments $\vec{m}$, and the particle concentration ϕ. To achieve mathematical closure, the distribution of the magnetic field must also be determined. This is provided by the magnetostatic form of Maxwell's equations, which govern the induced field inside the tube:

$$\vec{\nabla}\cdot\left(\vec{\tilde{H}}+\frac{M_d}{H_0}\vec{m}\right) = 0 \tag{7}$$

$$\vec{\nabla}\times\vec{\tilde{H}} = \vec{0} \tag{8}$$

where M_d is the domain magnetization of the MNPs, and the term $M_d\vec{m}$ corresponds to the magnetization vector normalized by H_0.

At the lateral boundary of the tube, S_2, the continuity of the normal and tangential components of the magnetic field between the internal (induced) and applied fields must be satisfied:

$$\vec{H}\cdot\vec{n}_2 = \vec{H}_0\cdot\vec{n}_1 \tag{9}$$

$$\vec{H}\times\vec{n}_2 = \vec{H}_0\times\vec{n}_1 \tag{10}$$

At the inlet S_1 and outlet S_3, zero normal flux is imposed for the magnetic field:

$$\vec{\nabla}\otimes\vec{H}\cdot\vec{n}_{1,3}\Big|_{S_{1,3}} = 0 \tag{11}$$

The transport dynamics of MNPs and the macroscopic orientation of their magnetic moments are described by a probability density function $\Psi(\vec{x}, \vec{u}, t)$, governed by the Smoluchowski kinetic equation. This equation accounts for both translational and rotational diffusion of the particles, while also incorporating the effects of Brownian motion, the external magnetic field, and hydrodynamic interactions between the fluid and the particles.

$$\frac{\partial\Psi}{\partial t}+\vec{v}\cdot\vec{\nabla}\Psi+\vec{\omega}_p\cdot\vec{\mathscr{L}}_u\Psi = \mathscr{D}\left[\nabla^2\Psi-\alpha\vec{\nabla}\cdot\left(\Psi\vec{\nabla}\left(\vec{u}\cdot\vec{\tilde{H}}\right)\right)\right] + \mathscr{D}_u\left[{\nabla_u}^2\Psi-\alpha\vec{\mathscr{L}}_u\cdot\left(\Psi\vec{\mathscr{L}}_u\left(\vec{u}\cdot\vec{\tilde{H}}\right)\right)\right] \tag{12}$$

Here, $\vec{v}$ denotes the velocity field, and $\vec{u}$ is the unit vector representing the particle orientation on the unit sphere ϖ. The operator $\vec{\mathscr{L}}_u = \vec{u}\times\nabla_u$ is the angular surface gradient on ϖ. $\mathscr{D} = \frac{K_BT}{6\pi\mu R_p}$ is the Stokes–Einstein translational diffusion coefficient, $\mathscr{D}_u = \frac{K_BT}{8\pi\mu {R_p}^3}$ is the rotational diffusion coefficient, and $\alpha = \frac{\mu_0 M_d H_0 V_p}{K_BT}$ is the Langevin parameter. The spin field is

defined as $\vec{\omega}_p = \vec{\Omega} + \mathscr{D}_u \alpha \vec{m} \times \vec{\vec{H}}$, with $\vec{\Omega} = \frac{1}{2}\vec{\nabla} \times \vec{v}_l$ the vorticity field.

Because the Smoluchowski eqn (12) is posed in a five-dimensional phase space (x, y, z, θ, φ), direct solutions are intractable. To overcome this, the probability density is approximated by a truncated moment expansion.[40–42] In this formulation, the zeroth-order moment corresponds to the particle concentration, while the first-order moment characterizes the macroscopic alignment of the particles' magnetic moments:

$$\Psi(\vec{x}, \vec{u}, t) = \frac{\phi(\vec{x}, t)}{4\pi} + \frac{3}{4\pi}\vec{u} \cdot \vec{m}(\vec{x}, t) \tag{13}$$

Based on this expansion, the zeroth moment of the Smoluchowski equation yields the mass conservation equation for the MNPs:

$$\frac{\partial \phi}{\partial t} + \vec{v} \cdot \vec{\nabla}\phi = \mathscr{D}\left(\nabla^2 \phi - \alpha \vec{\nabla} \cdot \left(\vec{m} \cdot \vec{\nabla}\vec{\vec{H}}\right)\right) \tag{14}$$

While the first moment provides the governing equation for the orientation of the particles' magnetic moments:

$$\frac{\partial \vec{m}}{\partial t} + \vec{v} \cdot \vec{\nabla}\vec{m} = \mathscr{D}\left(\nabla^2 \vec{m} - \frac{\alpha}{3}\vec{\nabla} \cdot \left(\phi \vec{\nabla}\vec{\vec{H}}\right)\right) + \vec{\omega}_p \times \vec{m} + \frac{1}{\tau_B}\left(\phi \frac{\alpha}{3}\vec{\vec{H}} - \vec{m}\right) \tag{15}$$

where $\tau_B = 2/\mathscr{D}_u$ is the Brownian relaxation time.

This derivation shows that the MNPs transport eqn (14) does not arise from an *ad hoc* assumption, but rather, it is a direct consequence of the Smoluchowski kinetic framework. Specifically, the zeroth moment of the distribution function yields an advection–diffusion equation for particle concentration in the dilute, clusterless regime. This clarifies that the advection–diffusion formulation used here is theoretically sound and consistent with previous studies of colloidal suspensions.[43–46]

The low translational diffusion coefficient of MNPs, typically on the order of $\mathscr{O}(10^{-11})$ m^2 s^{-1}, makes the contribution of the magneto-diffusive flux, $\alpha\nabla \cdot \left(\vec{m} \cdot \nabla\vec{\vec{H}}\right)$, negligible for both particle transport and magnetic moment orientation.[34,35] Consequently, the normalization condition for the probability density function,

$$\frac{1}{\phi_0}\int_{V_t}\int_{\varpi} \Psi \mathrm{d}u \mathrm{d}V = 1 \equiv \int_{V_t} \phi = \phi_0, \tag{16}$$

where ϕ_0 is the injected volume fraction of the MNPs and V_t is the total channel volume, can be omitted. Based on these simplifications, eqn (14) and (15) reduce to:

$$\frac{\partial \phi}{\partial t} + \vec{v} \cdot \vec{\nabla}\phi = \mathscr{D}\nabla^2 \phi \tag{17}$$

$$\frac{\partial \vec{m}}{\partial t} + \vec{v} \cdot \vec{\nabla}\vec{m} = \mathscr{D}\nabla^2 \vec{m} + \vec{\omega}_p \times \vec{m} + \frac{1}{\tau_B}\left(\phi \frac{\alpha}{3}\vec{\vec{H}} - \vec{m}\right) \tag{18}$$

The transport equation for the nanoparticle concentration, eqn (17), is subject to three boundary conditions. At the wall S_2, a no-flux condition is imposed:

$$\vec{\nabla}\phi \cdot \vec{n}_2\Big|_{S_2} = 0 \tag{19}$$

At the inlet and outlet, the Danckwerts boundary conditions[47] are applied, corresponding to a closed–closed system:[48]

$$\left(-\mathscr{D}\vec{\nabla}\phi + \vec{v}\phi\right) \cdot \vec{n}_1{}^+\Big|_{S_1} = \vec{v}_l \phi \cdot \vec{n}_1{}^-|_{S_1} \tag{20}$$

$$\vec{\nabla}\phi \cdot \vec{n}_3\Big|_{S_3} = 0 \tag{21}$$

The initial condition corresponds to the injection of a dilute ferrofluid pulse at $t = 0$, prescribed as a Gaussian distribution along the axial direction and uniform over the cross-section:

$$\phi(\vec{x}, t = 0) = \phi_0 \frac{\exp\left[-\frac{z^2}{2\sigma^2}\right]}{\frac{1}{L}\int_0^L \exp\left[-\frac{z^2}{2\sigma^2}\right]\mathrm{d}z}, \tag{22}$$

where ϕ_0 is the average value imposed on the pulse over the entire tube volume. $\vec{x} = (x, y, z)$ denotes the spatial coordinates. The parameter σ was adjusted such that the initial plug occupies approximately $L/50$ of the tube length. This formulation avoids the nonphysical singularity of a step-like injection and ensures a finite, physically meaningful nanoparticle concentration at the inlet.

Regarding the orientation equation (eqn (18)), a zero-flux condition is imposed on all surfaces:

$$(\nabla \vec{m}) \cdot \vec{n}_i|_{S_i} = \vec{0} \quad i = 1, 2, 3 \tag{23}$$

In this study, we consider high-frequency RMFs, under which a magnetocaloric effect may arise during the transport of MNPs inside the tube. The macroscopic energy balance in this case can be expressed as:[49]

$$\left(\rho_l c_{p,l}(1 - \phi) + \rho_p c_{p,p}\phi\right)\frac{\partial T}{\partial t} + \rho_l c_{p,l}\vec{\nabla} \cdot (\vec{v}T) = k_l \nabla^2 T + \mu_0 M_d \omega_0 \mathrm{Re}\left\{\vec{\underline{H}}\right\} \cdot \mathrm{Re}\{j\vec{\underline{m}}\} \tag{24}$$

where ρ_l and ρ_p are the densities of the liquid and the nanoparticles, $c_{p,l}$ and $c_{p,p}$ are their respective heat capacities, T is the fluid temperature, k_l is the thermal conductivity of the liquid, and ω_0 is the angular frequency of the applied RMF. Re stands for the real part of a complex quantity, and j is the imaginary unit ($j^2 = -1$). The last term on the right-hand side represents the heat generated by the phase-lagged response of the magnetic moments to the oscillating field.

A zero heat flux condition is imposed on all boundaries:

$$\vec{\nabla}T \cdot \vec{n}_i\Big|_{S_i} = 0 \quad i = 1, 2, 3 \tag{25}$$

Temperature variations directly influence both the viscosity of the carrier liquid and the domain magnetization of the MNPs. In the present work, the carrier liquid is water, for which the temperature-dependent viscosity is expressed as:[50]

$$\mu(T) = a_1 \exp\left(\frac{a_2}{T} + a_3 T + a_4 T^2\right), \tag{26}$$

with $a_1, \ldots, a_4$ denoting empirical fitting constants. For water, the coefficients are: $a_1 = 1.865 \times 10^{-14}$, $a_2 = 4209$, $a_3 = 0.04527$, and $a_4 = -3.376 \times 10^{-5}$.

As for the temperature dependence of the domain magnetization, Bloch's law predicts a quadratic T^2 decrease of M_d with temperature:[51]

$$M_d(T) = M_d(0)(1 - BT^2), \quad (27)$$

where $M_d(0)$ is the domain magnetization at 0 K, and B is the Bloch constant.

In this study, we focus on cobalt ferrite nanoparticles ($CoFe_2O_4$). For this material, the Bloch constant B decreases with particle size and converges toward the bulk value $B = 1.576 \times 10^{-6}$ K^{-2}, while $M_d(0)$ increases with particle size, asymptotically reaching the bulk magnetization $M_d(0) = 510$ kA m^{-1}.[51]

2.3 Pulsed scalar transport model

In addition to the transport of MNPs, we also consider the dispersion of a passive scalar, denoted by $C(\vec{x}, t)$, which is introduced into the system as an instantaneous pulse injection. Its governing equation is given by the standard advection–diffusion equation:

$$\frac{\partial C}{\partial t} + \vec{v} \cdot \vec{\nabla} C = \mathscr{D}_s \nabla^2 C, \quad (28)$$

where C is the scalar concentration and D_s is the molecular diffusion coefficient of the scalar.

It should be emphasized that eqn (14) and (28) govern two distinct species: the first describes the transport of MNPs, while the second corresponds to the passive scalar.

At the tube wall S_2, a no-flux condition is imposed:

$$\vec{\nabla} C \cdot \vec{n}_2 \Big| S_2 = 0. \quad (29)$$

At the inlet and outlet, we adopt the Danckwerts boundary conditions corresponding to a closed–closed system:[47]

$$\left(-D_s \vec{\nabla} C + \vec{v}_1 C\right) \cdot \vec{n}_1^{+} \Big| S_1 = \vec{v} C \cdot \vec{n}_1^{-} | S_1, \quad (30)$$

$$\vec{\nabla} C \cdot \vec{n}_3 \Big| S_3 = 0. \quad (31)$$

The initial condition corresponds to the injection of an instantaneous pulse of concentration C_0 at $t = 0$, represented by a Dirac delta distribution along the axial coordinate:

$$C(\vec{x}, t = 0) = C_0 \delta(z). \quad (32)$$

3 Results and discussion

In this section, we investigate the transport of an impulse in a cylindrical tube under laminar Poiseuille flow (Fig. 1). The lateral wall of the tube is subjected to an external magnetic field oriented perpendicularly to the surface (Fig. 1). Two magnetic configurations are considered: an SMF, oriented radially, and an RMF, rotating in the transverse plane. We first examine the dispersion of a single Dirac-like impulse of MNPs suspended in the carrier fluid, under either SMF or RMF, where the injected MNP concentration corresponds to a dilute, clusterless swarm. This analysis allows us to quantify the influence of magnetic forces—Kelvin body force and magnetic torque—on particle distribution and axial dispersion. In addition to purely hydrodynamic effects, the interaction of the MNPs with the time-dependent magnetic field, namely the RMF, can lead to local energy dissipation,[52] potentially causing slight temperature rises in the suspension. In a second step, we consider the simultaneous injection of two impulses: one consisting of MNPs and the other of a passive scalar. This configuration aims to evaluate how the magnetically induced modification of MNP transport impacts the dispersion of a non-magnetic solute sharing the same flow field.

The governing equations described in Section 2 are solved using the finite element method implemented in COMSOL Multiphysics (version 4.4). The computational domain is a cylindrical tube meshed with triangular elements in the cross-sectional plane, refined near the wall, and extruded along the axial direction. For the momentum equation, a P2–P1 discretization is adopted for the velocity and pressure fields, respectively, ensuring numerical stability for incompressible flow. All other equations are discretized with first-order Lagrange (P1) elements. A segregated iterative solver strategy (GMRES with algebraic multigrid preconditioning) was adopted to efficiently handle the coupled transport equations and ensure stable convergence. Time integration is carried out with the backward differentiation formula (BDF) and adaptive time stepping. Post-processing of the simulation data was performed *via* Python scripts to compute cross-sectional averages, variances, transverse velocity profiles, and contour maps used in the analysis and figures.

It should be noted that the magnetic forcing terms were not part of the default laminar flow module in COMSOL. The Kelvin body force and the magnetic torque were explicitly defined and introduced by us as volumetric source terms in the creeping-flow momentum equation. In addition, the magnetic field equations (Maxwell–Ampère and Maxwell–flux laws), together with the transport equation for the orientation of the MNP magnetic moments, were implemented through the general mathematics interface of COMSOL, ensuring full coupling between the flow and magnetic sub-problems.

To ensure stability and reliability, the transport equations including advective terms were solved using the built-in cross-wind stabilization scheme of COMSOL, and an axial discretization step of 2×10^{-6} was adopted to control numerical diffusion. Time integration was carried out with the backward differentiation formula (BDF) using adaptive time stepping, which automatically adjusts to the temporal evolution and prevents instabilities. Standard numerical checks (mesh refinement and time-step sensitivity) confirmed convergence of the simulations, and in the absence of a magnetic field the framework consistently reproduced the classical Taylor dispersion.

3.1 MNP transport under static magnetic fields

We first examine the case of an SMF oriented radially, with a constant magnitude $H_0 = 14.713$ kA m^{-1}, corresponding to a

Langevin parameter $\alpha = 1$. This field intensity is relatively low and can be readily achieved with standard laboratory electromagnets, as reported in previous experimental studies.[26,28] The mean flow velocity is set to $v_0 = 0.25$ mm s^{-1}, corresponding to a Reynolds number of order $\mathrm{Re} = \frac{2v_0R}{\nu} = 0.05$, which confirms that the flow is in the Stokes regime. The injected concentration of MNPs is $\phi_0 = 5 \times 10^{-5}$. At this dilute level, dipole–dipole interactions can be neglected, and the system is therefore assumed to operate in a clusterless regime, where the MNPs behave as independent Brownian particles. The MNPs have an average diameter of $D_p = 10$ nm and a domain magnetization $M_d = 425$ kA m^{-1}. Under these conditions, the translational diffusion coefficient of the MNPs $\mathscr{D}$ is small, leading to a particle Péclet number $\mathrm{Pe} = 2v_0R/\mathscr{D} = 1145$, which indicates that axial advection largely dominates over diffusion.

The temporal evolution of the cross-sectionally averaged MNP concentration at $z = L/2$ and $z = L$ is reported in Fig. 2. In the absence of a magnetic field, the concentration profile exhibits a pronounced asymmetry: the signal rises sharply to a peak value, followed by a slower decay, resulting in a long trailing tail. This behavior reflects the dominance of axial advection over molecular diffusion for the present Péclet number (Pe = 1145). The parabolic velocity profile of Poiseuille flow causes the initially compact pulse to deform as it travels downstream. Fluid elements near the tube axis, where the velocity is maximal, transport MNPs rapidly and contribute to the early sharp rise in concentration. Conversely, particles near the wall, where the local velocity is much lower, arrive later at the observation plane, producing the extended tail of the signal. The resulting radial concentration gradients are a direct consequence of the shear-induced stretching of the pulse within the laminar flow field. The outlet signal in Fig. 2 displays a small left shoulder, *i.e.*, a weak rise in concentration preceding the main peak. Such a feature is a known outcome of laminar Poiseuille flow at a high Péclet number in the absence of any magnetic field, as previously reported in the context of passive scalar dispersion.[53,54] In purely hydrodynamic conditions, it originates from the faster advection of particles near the tube axis relative to those close to the wall, producing an early arrival of a small colloidal fraction of the injected pulse.

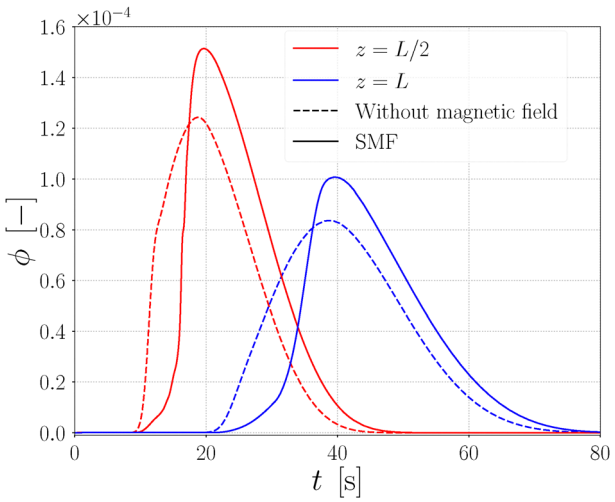

Fig. 2 Temporal evolution of the cross-sectionally averaged MNP concentration at $z = L/2$ and $z = L$ for an inlet velocity $v_0 = 0.25$ mm s^{-1} (Pe ≈ 1145, Re ≈ 0.05), comparing the cases without a magnetic field and with an SMF ($\alpha = 1$, $H_0 = 14.713$ kA m^{-1}). The injected concentration is $\phi_0 = 5 \times 10^{-5}$; particle diameter $D_p = 10$ nm; domain magnetization $M_d = 425$ kA m^{-1}.

The activation of the SMF produces noticeable changes in the concentration signals at both observation planes. A clear reduction in the variance is observed, primarily due to the increase in peak amplitude compared to the no-field case. In addition, the trailing behavior of the signal is slightly attenuated. These two effects indicate that the MNP pulse undergoes a contraction, suggesting the presence of an additional mechanism that reduces the radial concentration gradients induced by the parabolic Poiseuille profile. In the SMF configuration, the magnetic torque term $\frac{K_B T}{V_p}\alpha\vec{m} \times \vec{H}$, eqn (2), which drives spin-up flows, is absent, as it requires an RMF to be activated. Therefore, the only mechanism capable of generating a secondary transverse flow in this case is the Kelvin body force term $\frac{K_B T}{V_p}\alpha\vec{m} \cdot \vec{\nabla} \otimes \vec{H}$, eqn (2). This force drives MNP migration toward regions of higher magnetic field magnitude, thereby redistributing particles radially and mitigating the shear-induced stretching of the pulse.

The mechanism behind the KBF in this configuration can be understood by recalling the analysis of Larbi *et al.*,[34] who investigated passive scalar mixing in a Y-shaped tube containing MNPs and subjected to an RMF. In their study, when MNPs were injected from both inlets, only the spin-up flow driven by the magnetic torque term $\frac{K_B T}{V_p}\alpha\vec{m} \times \vec{H}$ was observed, with no contribution from the KBF. This is consistent with the projection of the linear momentum equation, eqn (2), onto the radial direction, which shows that the KBF term acts in a hydrostatic manner, similar to gravity:

$$\frac{\partial P}{\partial r} = \frac{K_B T}{V_p}\alpha\vec{m} \cdot \vec{\nabla} \otimes \vec{H}, \tag{33}$$

where $\vec{m} = \phi\vec{p}$ and $\vec{p}$ is the polarization vector.

In the absence of MNP concentration gradients, the radial pressure variations induced by the KBF are exactly balanced by symmetry, leading to $\Delta P = 0$ across the cross-section. Consequently, no transverse flow is generated. To activate the KBF, a finite gradient of MNP concentration across the cross-section is required. In the Y-shaped configuration, this was achieved by injecting MNPs from only one branch, creating an asymmetric particle distribution and a non-zero cross-sectional $\Delta P_\perp \neq 0$, which in turn induced a transverse convective flow.[34] As discussed in Section 1, in the absence of cross-sectional MNP concentration gradients, the transverse (crosswise) pressure variations induced by the KBF cancel by symmetry, resulting in $\Delta P_\perp = 0$ and no transverse flow generation. This is distinct from the axial pressure drop $\Delta P_\parallel$, which is always

present to drive the bulk flow. An MNP concentration gradient across the section is therefore required to activate the KBF, as it produces a non-zero $\Delta P_{\perp}$ that drives convection perpendicular to the main flow direction.

The same principle applies here to Taylor dispersion. The Poiseuille flow naturally generates transverse concentration gradients as the pulse is stretched—fast-moving particles near the center advance ahead of those near the wall. These gradients, in the presence of an SMF, generate a dynamic pressure difference across the section *via* the KBF, which drives a transverse flow. This secondary flow acts to reduce the concentration gradients created by the parabolic velocity profile, pushing the system back toward an equilibrium state with a more uniform radial distribution. This explains the observed reduction in the variance of the concentration signal in Fig. 2. To visualize the secondary flow induced by the KBF, Fig. 3 shows the transverse velocity magnitude $\sqrt{v_x^2 + v_y^2}$ at $z = L/2$ for different times (14, 16, 18, 20 s). At t = 14 s, Fig. 4a, the maximum transverse velocity is 11 μm s^{-1}, corresponding to the arrival of MNPs with a relatively small concentration gradient. At t = 16 s, Fig. 4b, the transverse velocity reaches 90.6 μm s^{-1}, coinciding with the passage of a strong radial concentration gradient. For t = 18 s and 20 s, Fig. 4c and d, the transverse velocity decreases as the gradients weaken. The effect of the KBF is strictly localized to the region where MNPs are present; once the pulse has passed, the transverse velocity field returns to its initial zero state.

It is worth noting that although the MNP concentration in this case is dilute ($\phi_0 \approx 10^{-5}$), the influence of the KBF remains significant. This is consistent with the experimental findings of Leong *et al.*,[55] who reported convection driven by magnetic body forces at concentrations as low as 5 mg L^{-1} (corresponding to $\phi_0 \approx 10^{-6}$). Their results demonstrated that such dilute suspensions can still experience measurable hydrodynamic effects, including enhanced homogenization and accelerated collection. These observations support the validity of our modeling assumptions and confirm that Kelvin body forces can play a key role even in dilute colloidal systems.

To better illustrate the secondary flow generated across the cross-section, Fig. 3e shows the temporal evolution of the velocity component v_x as a function of y along the line $x = 0$ in the plane $z = L/2$, for t = 13, 14.5, 15.5, 19.5, 44 s. This representation highlights the local action of the KBF in a clearer manner than the magnitude plots. The space–time between $z = 0$ and $z = L/2$ is 20 s, defining the reference time before the pulse arrives at the observation plane. At t = 13 s, the v_x profile indicates the very beginning of the pulse arrival, with a small transverse motion. At t = 14.5 s, v_x reaches its maximum magnitude (≈ -23 μm s^{-1}), pointing in the negative direction. Remarkably, just one second later (t = 15.5 s), the velocity completely reverses its sign, reaching $\approx +20$ μm s^{-1}. These two instants correspond to the arrival of a significant amount of MNPs with intense radial concentration gradients. The rapid sign reversal of v_x reflects the strongly three-dimensional nature of the secondary flow generated by the KBF, consistent with similar effects reported in Larbi *et al.*[34] By t = 19.5 s, the transverse velocity magnitude decreases compared to earlier peaks, indicating the beginning of the MNP plug's departure from the observation plane and the associated reduction of concentration gradients due to axial transport. Finally, at t = 44 s, the v_x profile is essentially flat, confirming the complete disappearance of MNPs from this location and the cessation of KBF-induced motion.

To further highlight the link between MNP concentration gradients and the transverse flow generated by the Kelvin body force, Fig. 4 presents the cross-sectional concentration contours of MNPs at $z = L/2$ for the same time instants as in Fig. 3 (t = 14, 16, 18, 20 s). In the absence of a magnetic field, the concentration distribution remains symmetric with respect to the tube axis, reflecting the symmetry of the underlying Poiseuille velocity profile. Under SMF, however, the concentration field becomes clearly asymmetric. This loss of symmetry directly corresponds to the 3D distribution of the transverse velocity field shown in Fig. 3. At t = 14 s, Fig. 4a, the concentration contours are only weakly distorted, consistent with the low transverse velocity magnitude observed at this time. At t = 16 s, Fig. 4b, a pronounced asymmetry emerges, coinciding with the maximum transverse velocity and indicating the presence of strong radial concentration gradients. As time progresses t = 18, 20 s, Fig. 4c and d, both the asymmetry and the transverse velocities decrease as the MNP plug moves downstream and the concentration gradients relax. This direct correlation between the spatial distribution of MNPs and the induced transverse flow confirms that the KBF is only active in regions where significant radial concentration gradients of MNPs exist.

To evaluate the influence of the KBF on axial momentum transport, Fig. 5 shows the axial velocity v_z profiles along y at $x = 0$ in the cross-section located at $z = L/3$. The space–time between $z = 0$ and $z = L/3$ is 13.33 s. At t = 9 s, before the arrival of the MNP pulse, the velocity profile exhibits the parabolic shape characteristic of fully developed Poiseuille flow, as expected for a particle-free liquid. At t = 10.8 s, however, the profile is drastically altered: the axial velocity at the centerline ($y = 0$) drops to nearly half of its pre-perturbation value, while the velocities near the wall remain almost unchanged. This results in an inverted curvature, with near-wall velocities exceeding those at the center, a complete departure from the classical parabolic profile. This distortion indicates a modification of the axial momentum during the passage of the MNPs. The axial distribution of the particles, combined with the action of the KBF, decelerates the core flow while relatively accelerating the fluid near the walls. At t = 12 s, the profile recovers its initial parabolic shape, indicating the MNP pulse has departed this location and the KBF effect has ceased. This transient distortion shows that the KBF not only redistributes particles, but also actively perturbs the axial momentum field. This feature is unique to pulsed injections and absent under continuous MNP injection.

However, an important question arises in the context of Fig. 5: in this configuration, the magnetic field is oriented perpendicularly to the tube wall, meaning there is no axial

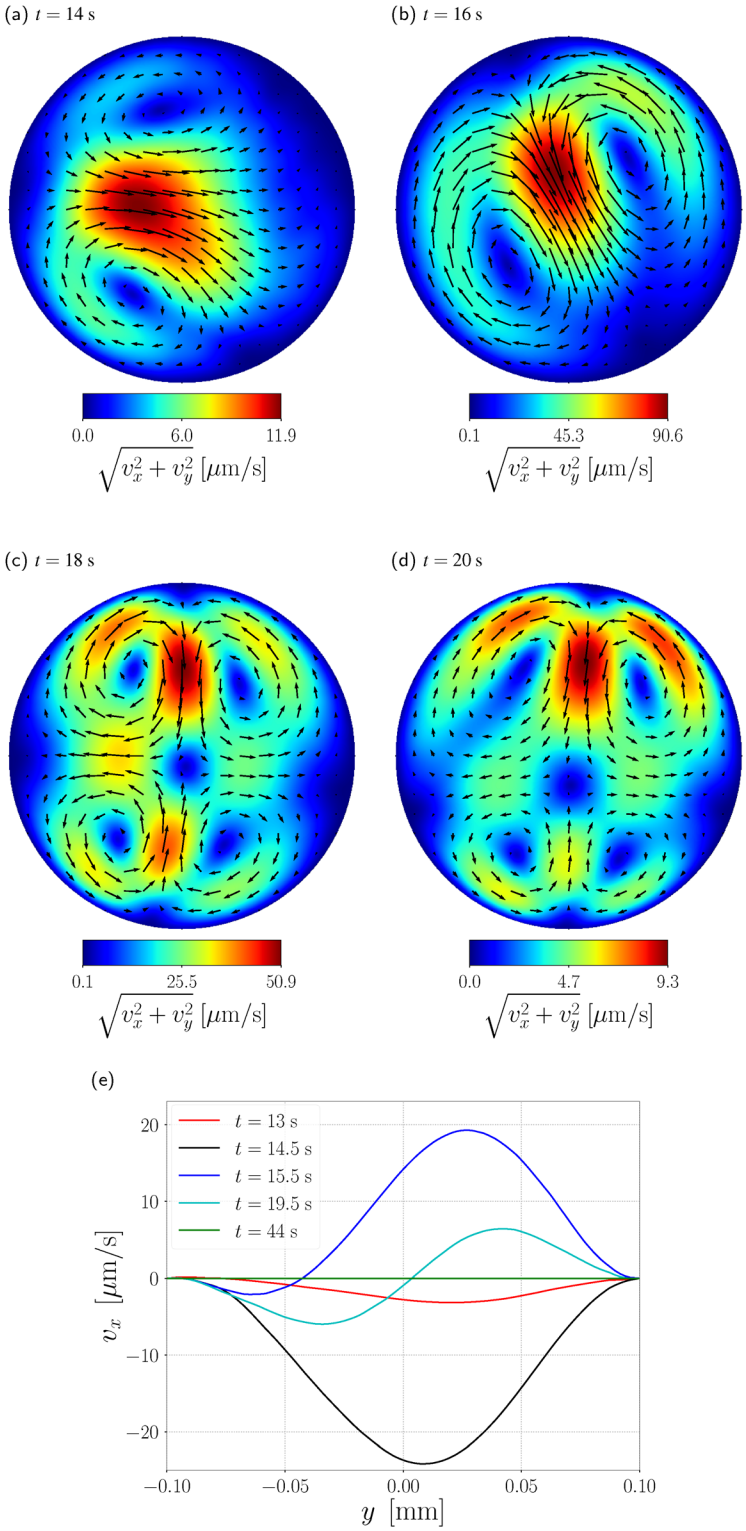

Fig. 3 (a)–(d) Evolution of the transverse velocity magnitude $\sqrt{v_x^2 + v_y^2}$ at $z = L/2$ under an SMF ($\alpha = 1$, $H_0 = 14.713$ kA m^{-1}), showing the secondary flow induced by the KBF during the passage of the MNP pulse. (e) Transverse velocity profiles $v_x(y)$ at $z = L/2$ and at different times under the same conditions. The KBF induces a transverse convective flow across the plug. Parameters common to all sub-figures: $v_0 = 0.25$ mm s^{-1} (Pe $\approx$ 1145, Re $\approx$ 0.05); injected concentration $\phi_0 = 5 \times 10^{-5}$; particle diameter $D_p = 10$ nm; domain magnetization $M_d = 425$ kA m^{-1}.

magnetic field component capable of producing a Kelvin body force in the z-direction ($\frac{K_B T}{V_p} \alpha \vec{m} \cdot \vec{\nabla} \otimes \vec{H}$ along z). In the study by Boroun and Larachi,[31] dealing with passive scalar mixing in a Taylor-dispersion configuration under a rotating magnetic

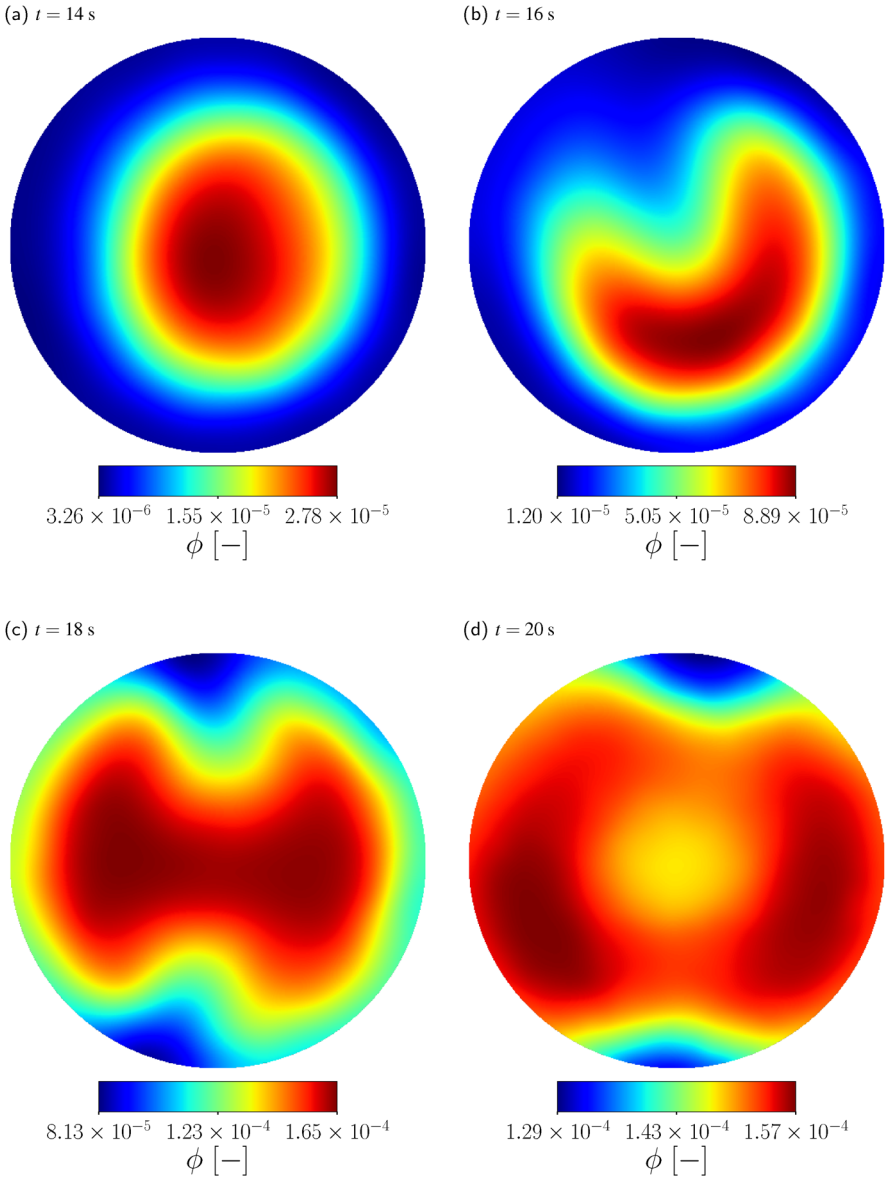

Fig. 4 Cross-sectional MNP concentration contours at $z = L/2$ and times (a) $t = 14$ s, (b) $t = 16$ s, (c) $t = 18$ s, and (d) $t = 20$ s, showing the loss of symmetry under an SMF ($\alpha = 1$, $H_0 = 14.713$ kA m^{-1}). Parameters: $v_0 = 0.25$ mm s^{-1} (Pe $\approx$ 1145, Re $\approx$ 0.05); injected concentration $\phi_0 = 5 \times 10^{-5}$; particle diameter $D_p = 10$ nm; domain magnetization $M_d = 425$ kA m^{-1}.

field, the concentration measurements showed no evidence of a change in the axial transport velocity of the momentum. Likewise, Larbi *et al.*[34] numerically confirmed that, for a Y-shaped tube continuously supplied with MNPs, the axial component of the momentum remained unaffected. The common feature of these two studies is the continuous injection of MNPs, which maintains a steady concentration distribution along the flow. In contrast, in the present configuration, MNPs are injected as a finite pulse, creating strong gradients in MNP concentration.

To clarify the origin of the axial velocity distortion observed in Fig. 5, we examine the *yz*-plane contours in Fig. 6. Fig. 6b shows v_z at $t = 10$ s. Throughout most of the tube, the flow retains the classical Poiseuille pattern, except in the region occupied by the MNP pulse. There, the same phenomenon seen in Fig. 5 appears: at the centerline ($y = 0$), v_z is lower than near the walls, while upstream of this point, the axial velocity increases slightly to compensate for the reduction, as clearly visible in Fig. 6b. To relate this to the MNP distribution, Fig. 6c presents the particle concentration in the same plane. The distortion of v_z occurs exactly at the head of the MNP plug, where the concentration is highest. Due to the initial parabolic velocity profile, the fastest-moving particles travel along the centerline, producing a strong axial concentration gradient along z at the plug head. This gradient can modify the axial momentum transport. Although there is no magnetic field component along z to directly produce a KBF in the axial direction, Fig. 6d shows that the KBF in the y-direction exhibits significant axial variation within the plug. Following the

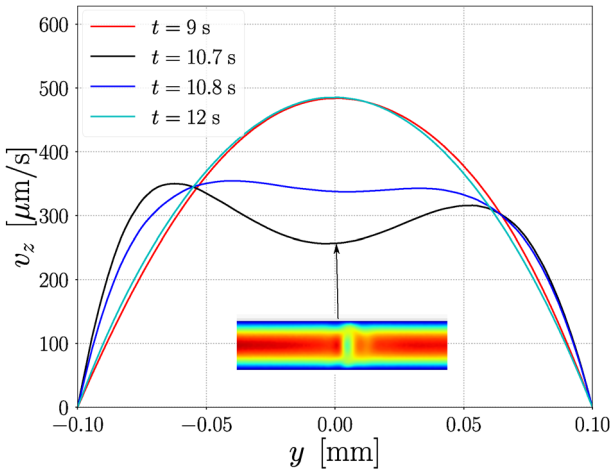

Fig. 5 Axial velocity profiles $v_z(y)$ at $x = 0$ and $z = L/3$ under an SMF ($\alpha = 1$, $H_0 = 14.713$ kA m^{-1}), showing core flow deceleration and near-wall acceleration at the pulse head compared to Poiseuille flow. An inset illustrates the cross-section at $z = L/3$ and $t = 10.7$ s, indicating the contour of the velocity v_z in the yz plane. Parameters: $v_0 = 0.25$ mm s^{-1} (Pe $\approx$ 1145, Re $\approx$ 0.05); injected concentration $\phi_0 = 5 \times 10^{-5}$; particle diameter D_p = 10 nm; domain magnetization $M_d = 425$ kA m^{-1}.

mechanism described by Larbi *et al.*,[34] a transverse KBF acting on a region with non-uniform particle concentration generates transverse pressure gradients; if these gradients vary along z, they can indirectly modify the axial velocity field. In our case, the non-uniform KBF along y at the plug head produces axial variations in the transverse pressure, altering the axial momentum distribution. This effect is confirmed in Fig. 6e, which displays the pressure gradient in the yz-plane. Outside the MNP region, the axial pressure gradient is constant, sustaining the Poiseuille profile. Inside the plug, however, the pressure gradient varies along z: at the head and centerline ($y = 0$), it reaches 4.7 Pa m^{-1}, exceeding the value required for the Poiseuille flow, effectively "blocking" the core and reducing v_z at the center. Near the walls, the axial pressure gradient decreases, explaining the higher velocities observed there. Upstream of this point, the pressure gradient is slightly lower than the Poiseuille corresponding value, resulting in a local acceleration that compensates for the core deceleration to conserve the volumetric flow rate.

To illustrate the effect of the SMF, Fig. 7 displays the cross-sectional concentration contours of MNPs in the yz-plane at t = 14, 20, 25 s. In the no-field case, the pulse exhibits the classical Taylor deformation, elongated along z and smoothly shaped by the parabolic Poiseuille profile. Under SMF ($\alpha = 1$), the pulse becomes noticeably compacted, most prominently at its head, and its overall axial extent is reduced relative to the no-field case. This compaction reflects an effective mixing of MNPs across the cross-section, which reduces the concentration gradients otherwise imposed by the parabolic shear. Mechanistically, two coupled effects drive this behavior: (i) the KBF-induced transverse flow (Fig. 3), which redistributes particles radially, and (ii) the local modification of the axial velocity field v_z at the pulse head (Fig. 5 and 6), where an increased axial pressure gradient at the centerline temporarily slows the core while maintaining higher near-wall velocities. The resulting "core braking" at the pulse head, together with transverse recirculation, shortens and thickens the leading front compared to the Poiseuille-shaped front observed without the field. This trend is consistently observed at all three times in Fig. 7.

It should be noted that the reduced axial extent and the narrower breakthrough curves observed under SMF reflect a suppression of axial dispersion together with enhanced cross-sectional homogenization. In this sense, mixing refers to the elimination of concentration gradients across the section, achieved here through the combined action of KBF-induced transverse recirculation and the local modification of the axial velocity field at the pulse head.

3.2 Rotating magnetic field

We now consider the case of an RMF applied in the transverse plane. In this configuration, the magnetic torque term, $\frac{K_B T}{V_p}\alpha \vec{m} \times \vec{H}$, is active and can drive a spin-up flow in addition to the KBF. The simulations are performed with the same hydrodynamic and particle parameters as in the SMF case: mean inlet velocity $v_0 = 0.25$ mm s^{-1}, injected MNP concentration $\phi_0 = 5 \times 10^{-5}$, particle diameter $D_p = 10$ nm, and domain magnetization $M_d = 425$ kA m^{-1}. The RMF amplitude is fixed at $H_0 = 14.713$ kA m^{-1}, corresponding to a Langevin parameter $\alpha = 1$. The excitation frequency f_0 considered in this study can reach up to 1 MHz. These values are well within the range attainable by standard laboratory equipment, as experimental studies have reported oscillating magnetic fields reaching up to 2 MHz.[56] Under these conditions, the particle Péclet number remains Pe $\approx$ 1145, indicating that, as in the SMF case, axial advection dominates over molecular diffusion.

The temporal evolution of the cross-sectionally averaged MNP concentration at $z = L/2$ and $z = L$ for three different configurations (no field, SMF, RMF) is shown in Fig. 8. The no-field and SMF cases were analyzed earlier. As mentioned earlier, under SMF the pulse broadening is mitigated, leading to a lower signal variance, consistent with the transverse redistribution of particles and the plug compaction described previously.

With an RMF at $f_0 = 100$ kHz, the variance reduction is approximately twice as large as under SMF. This indicates the contribution of an additional mechanism: the rotating field exerts a torque on the MNPs, generating a spin-up flow. This torque-driven secondary flow further enhances radial mixing and increases plug compaction, thereby reducing axial dispersion more effectively than the SMF alone.

The contours of the transverse velocity magnitude at $z = L/2$ at times t = 14, 18, 22, 26 s are reported in Fig. 9. At $t = 14$ s, the flow exhibits a vortex structure characteristic of an incipient spin-up flow, though it has not yet fully developed. Since this time is less than the time it takes for the MNP pulse to travel from $z = 0$ to $z = L/2$ (20 s), only a small fraction of the pulse has reached the observation plane. This results in a relatively low maximum transverse velocity of 0.1075 mm s^{-1}. By t = 18 and 22 s, the spin-up vortex has fully formed, and the maximum

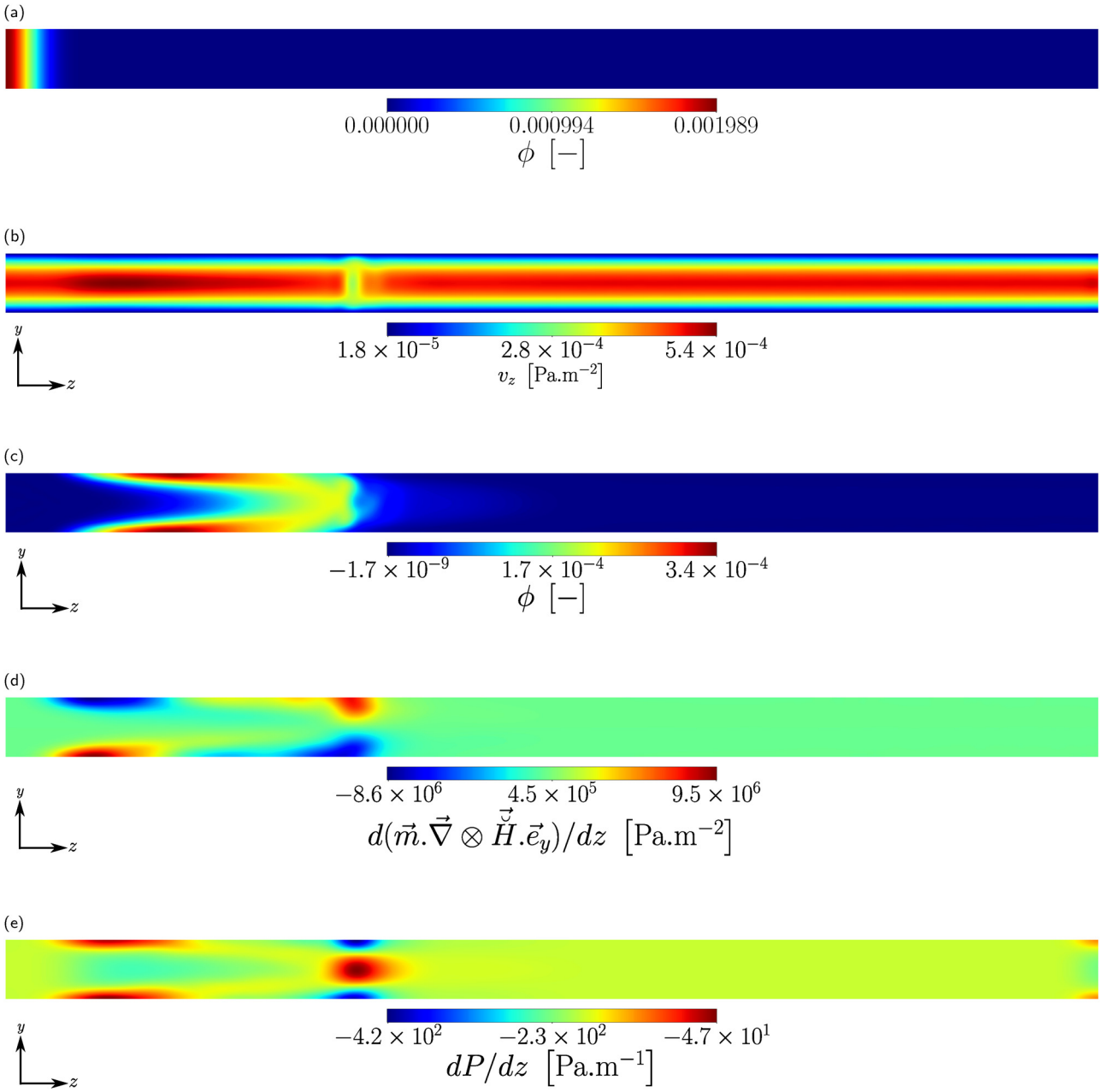

Fig. 6 Initial condition and flow/MNP distribution in the yz-plane under an SMF (α = 1, H_0 = 14.713 kA m^{-1}): (a) prescribed Gaussian concentration profile at the inlet (z = 0), used as the initial condition for the MNP pulse; (b) axial velocity at t = 10 s; (c) MNP concentration at t = 10 s; (d) axial variation of the transverse Kelvin body force at t = 10 s; and (e) axial pressure gradient at t = 10 s. Parameters: v_0 = 0.25 mm s^{-1} (Pe ≈ 1145, Re ≈ 0.05); injected concentration $\phi_0 = 5 \times 10^{-5}$; particle diameter D_p = 10 nm; domain magnetization M_d = 425 kA m^{-1}.

transverse velocity has increased sharply to 1.272 and 1.652 mm s^{-1}, respectively. These peaks correspond to the arrival of a large fraction of the pulse, when the concentration gradients are strongest. At t = 26 s, the maximum transverse velocity decreases to 0.675 mm s^{-1}, indicating that the particle concentration at $z = L/2$ is beginning to decline as the pulse moves downstream. Throughout all time frames, the velocity field retains the coherent vortex pattern of a spin-up flow. Unlike in the SMF case, which is characterized by a more three-dimensional structure, no visible signature of KBF-induced motion is observed. This is consistent with the magnitude of the velocities; even the smallest spin-up velocity (0.1075 mm s^{-1} at t = 14 s) exceeds the maximum velocity generated by the KBF under SMF conditions (0.0906 mm s^{-1}; see Fig. 3b).

The spin-up flow therefore completely overshadows any KBF effect. The highest spin-up velocity recorded (1.652 mm s^{-1}) is much greater than the mean transverse velocity in the SMF configuration. This implies that the spin-up flow timescale is much shorter than the dispersion timescale, allowing transverse gradients to be removed before axial dispersion can significantly develop. Effective suppression of Taylor-type

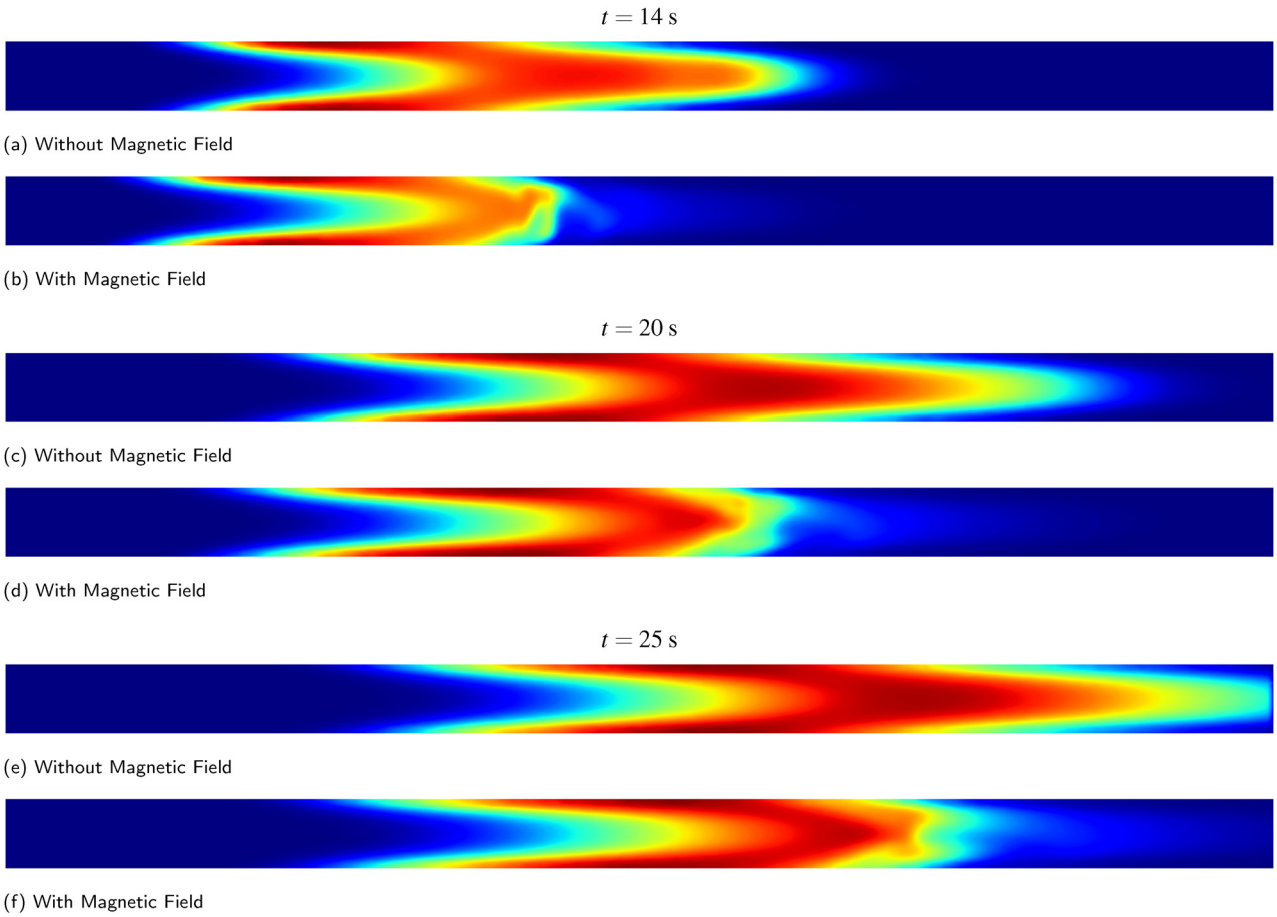

Fig. 7 MNP concentration contours in the yz-plane at (a) t = 14 s without SMF, (b) t = 14 s with SMF, (c) t = 20 s without SMF, (d) t = 20 s with SMF, (e) t = 25 s without SMF, and (f) t = 25 s with SMF (α = 1, H_0 = 14.713 kA m^{-1}), showing pulse compaction and deformation under SMF. Parameters: v_0 = 0.25 mm s^{-1} (Pe $\approx$ 1145, Re $\approx$ 0.05); injected concentration $\phi_0 = 5 \times 10^{-5}$; particle diameter D_p = 10 nm; domain magnetization M_d = 425 kA m^{-1}.

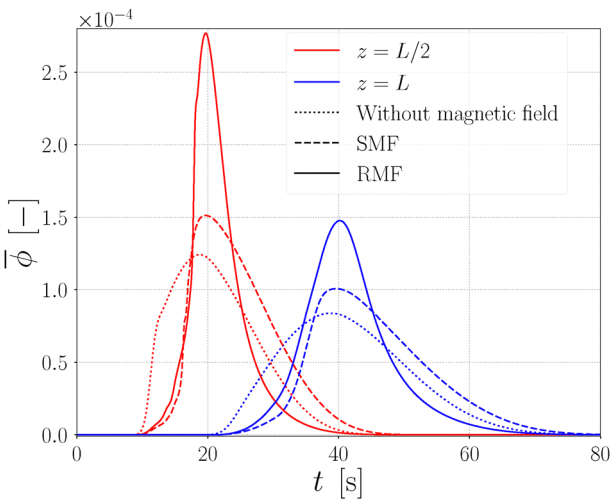

Fig. 8 Cross-sectionally averaged MNP concentration signals at $z = L/2$ and $z = L$ for no field, SMF, and RMF at f_0 = 100 kHz, showing enhanced variance reduction under RMF. Parameters: v_0 = 0.25 mm s^{-1} (Pe $\approx$ 1145, Re $\approx$ 0.05); H_0 = 14.713 kA m^{-1} (α = 1); injected concentration $\phi_0 = 5 \times 10^{-5}$; particle diameter D_p = 10 nm; domain magnetization M_d = 425 kA m^{-1}.

dispersion requires the spin-up velocity to exceed the mean Poiseuille velocity by several times.[33] In the present case, this condition is clearly satisfied, which explains the rapid erosion of transverse concentration gradients and the marked variance reduction observed in Fig. 8.

Fig. 9e presents the transverse velocity component v_x along y at $x = 0$ and $z = L/2$ for t = 12, 14, 18, 24, 29 s. These one-dimensional profiles complement the two-dimensional contours in Fig. 9, providing a more detailed view of the spin-up flow structure and its temporal evolution. At t = 12 and 14 s, the velocities remain low, indicating the early arrival of MNPs, although the antisymmetric shape of the profiles already reflects a developing spin-up vortex. At t = 18 and 24 s, the flow reaches its highest intensity, with peaks between 1 and 1.5 mm s^{-1}, corresponding to the passage of the pulse core where the MNP concentration, and thus magnetic torque, are strongest. By t = 29 s, the velocity decreases as the MNP concentration drops downstream. In all cases, the pattern is characteristic of a spin-up flow, with no evidence of the three-dimensional Kelvin body force motion seen under SMF. The dominance of the magnetic torque-driven vortex accounts for the rapid homogenization of radial concentration

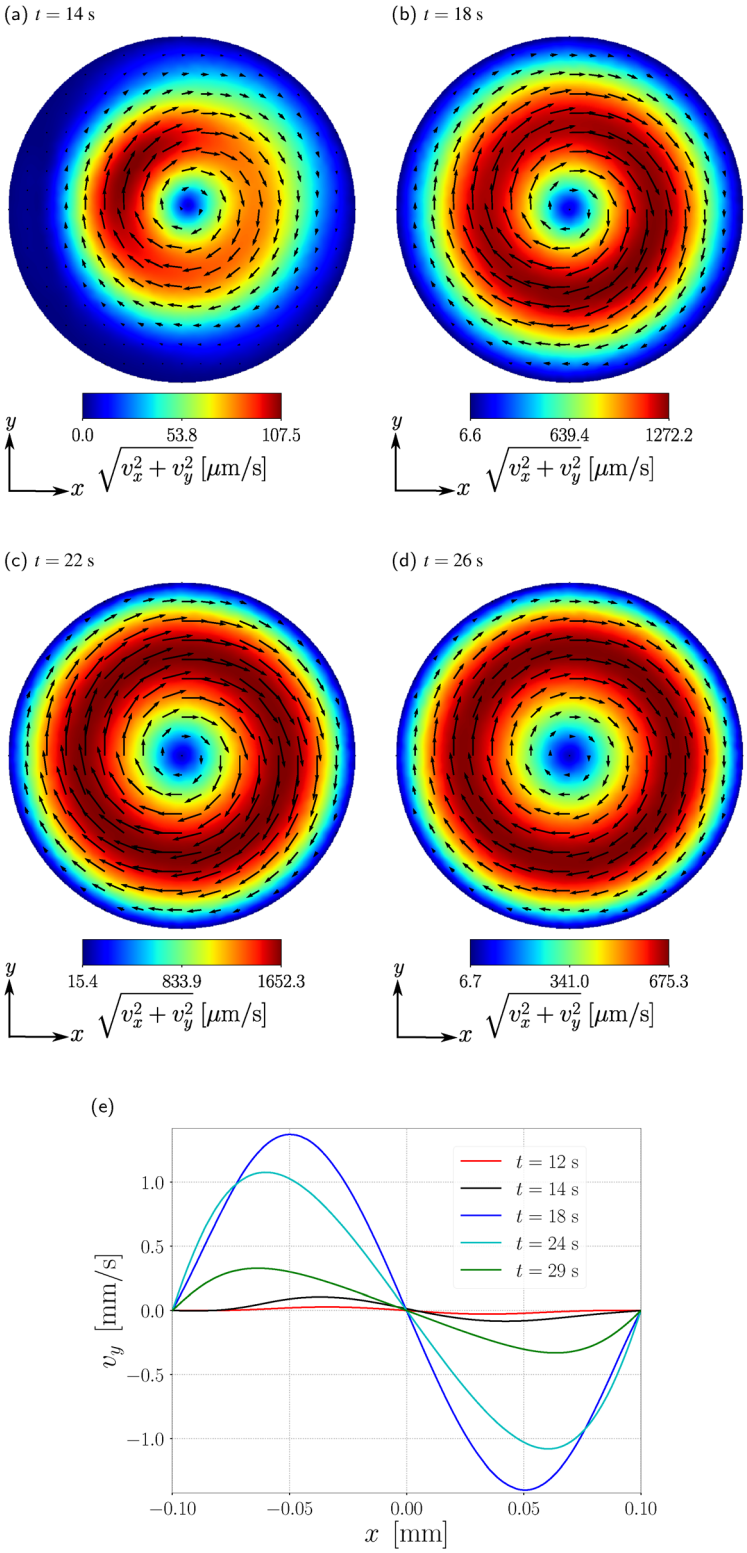

Fig. 9 (a)–(d) Transverse velocity magnitude contours at $z = L/2$ under an RMF (f_0 = 100 kHz), showing the evolution of the spin-up flow vortex at t = 14, 18, 22, 26 s. (e) Temporal evolution of the transverse velocity profile $v_y(x)$ at $x = 0$ and $z = L/2$ under the same conditions. Parameters common to all sub-figures: v_0 = 0.25 mm s^{-1} (Pe $\approx$ 1145, Re $\approx$ 0.05); H_0 = 14.713 kA m^{-1} ($\alpha = 1$); injected concentration $\phi_0 = 5 \times 10^{-5}$; particle diameter D_p = 10 nm; domain magnetization M_d = 425 kA m^{-1}.

gradients and the pronounced variance reduction observed in Fig. 8.

To investigate the action of the RMF on MNP transport along the tube, Fig. 10 presents the MNP concentration contours in

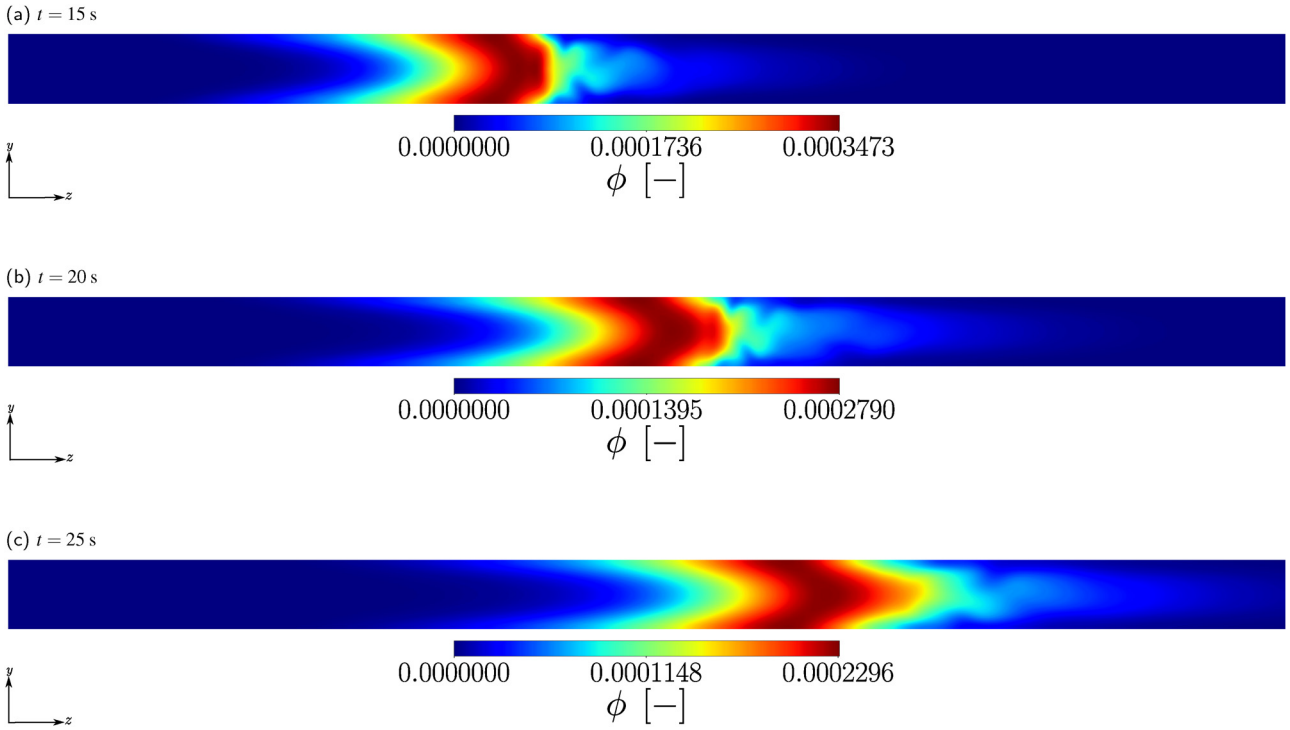

Fig. 10 MNP concentration field in the *yz*-plane under an RMF at f_0 = 100 kHz at (a) t = 15 s, (b) t = 20 s, and (c) t = 25 s. Parameters: v_0 = 0.25 mm s^{-1} (Pe ≈ 1145, Re ≈ 0.05); H_0 = 14.713 kA m^{-1} (α = 1); injected concentration $\phi_0 = 5 \times 10^{-5}$; particle diameter D_p = 10 nm; domain magnetization M_d = 425 kA m^{-1}.

the *yz*-plane at t = 15, 20, 25 s. Comparing the RMF case at t = 20 s, Fig. 10b, with the no-magnetic field case at the same time, Fig. 7c, reveals a pronounced reduction of the broadening length of the plug. This compression results from the strong attenuation of transverse concentration gradients, driven primarily by the intense mixing associated with the spin-up flow. A notable feature under RMF is the oscillatory deformation of the plug head over time. This unsteady behavior contrasts with the SMF case, where the head is progressively flattened, erasing the parabolic front shape. The difference stems from the nature of the RMF: the field rotates radially at high angular velocity. Considering the system's characteristic evolution time *versus* the RMF rotation period, even at low rotation rates (*e.g.*, 10 Hz) the RMF appears quasi-static in each transverse plane. Consequently, the RMF simultaneously possesses the properties of an SMF and, by virtue of its rotation, generates a magnetic torque that drives the spin-up flow.

As shown earlier for Fig. 9, the secondary flow induced by KBF is completely masked by the much stronger spin-up flow in the RMF case, making its contribution to transverse mixing negligible. The open question is whether the axial KBF effect, clearly identified for the SMF in Fig. 5 and 6, remains present under RMF conditions. To address this, Fig. 11 presents the axial velocity field v_z in the *yz*-plane at t = 15, 20, and 25 s.

At t = 15 s and t = 20 s, the results reveal the same core-blocking phenomenon observed in the SMF configuration: a marked reduction in v_z at the center of the plug head, combined with an upstream acceleration in the surrounding flow to conserve axial momentum. This blocking is the signature of an axial KBF effect, caused by local variations in the axial pressure gradient along the plug. It is more pronounced at t = 15 s corresponding to the early stage of plug compression than at t = 20 s, when the head has partially flattened. At t = 25 s, the blocking pattern disappears, but the contours show clear spatial oscillations of v_z across the plug head. These oscillations correspond to the wavy concentration patterns already identified in Fig. 10 under RMF, suggesting a dynamic interaction between the magnetic torque–driven vortex and the axial momentum redistribution. Overall, Fig. 9 and 11 show that the RMF not only reproduces the SMF-like axial KBF effect, altering the axial momentum distribution and contributing to plug compaction, but also superimposes a strong magnetic torque that generates the spin-up flow and dominates transverse mixing. The coexistence of these two mechanisms under RMF conditions explains the much greater shortening of the plug and the faster elimination of transverse concentration gradients compared to the SMF case.

We now turn to the influence of MNP concentration on plug transport, focusing on the outlet signal as an indicator of plug behavior. Fig. 12 shows the outlet concentration signal, which is normalized by the injected MNP concentration and averaged over the cross-section, at f_0 = 100 kHz. The figure compares the effects of varying the injected MNP concentration under RMF and no-field conditions. The results indicate that the outlet signal is highly sensitive to the quantity of injected MNPs. For $\phi_0 = 1 \times 10^{-4}$, the signal variance is notably lower, and the

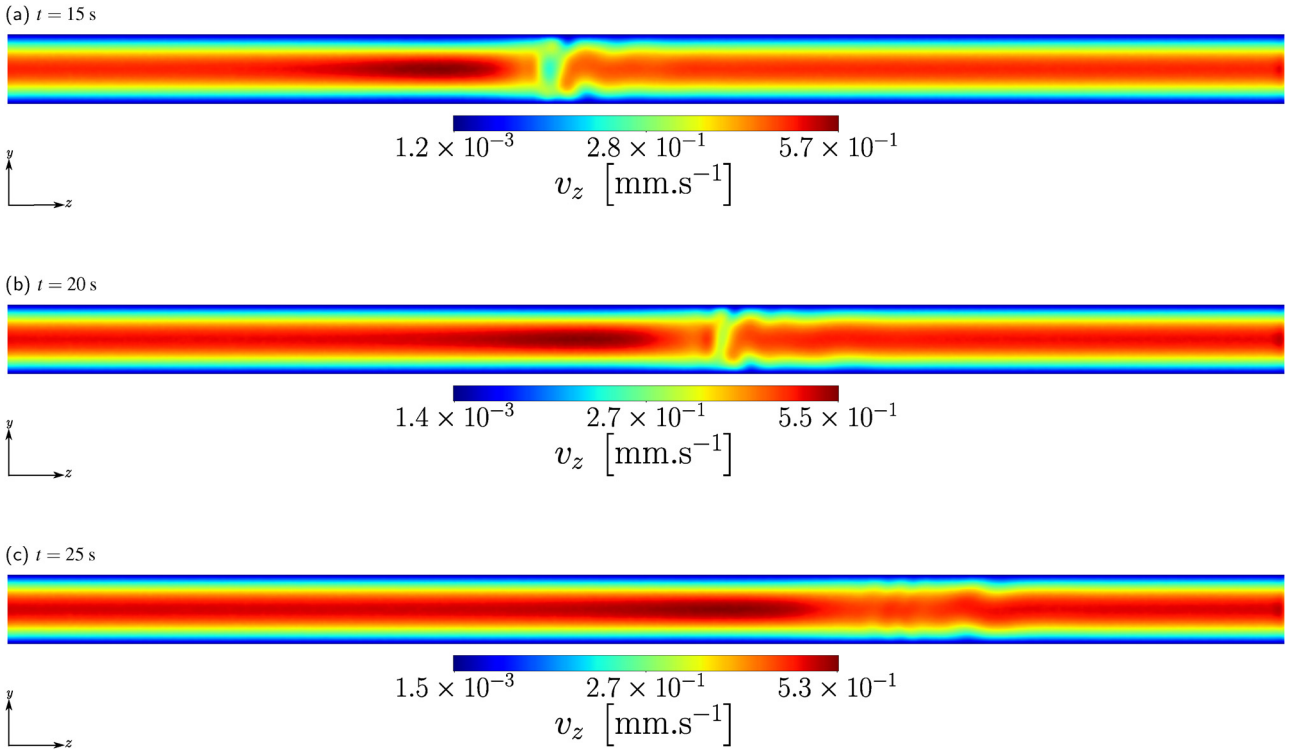

Fig. 11 Contour plots of the axial velocity component v_z in the yz-plane at x = 0, shown at (a) t = 15 s, (b) t = 20, and (c) t = 25 s under an RMF (f_0 = 100 kHz). Parameters: v_0 = 0.25 mm s^{-1} (Pe ≈ 1145, Re ≈ 0.05); H_0 = 14.713 kA m^{-1} (α = 1); injected concentration $\phi_0 = 5 \times 10^{-5}$; particle diameter D_p = 10 nm; domain magnetization M_d = 425 kA m^{-1}.

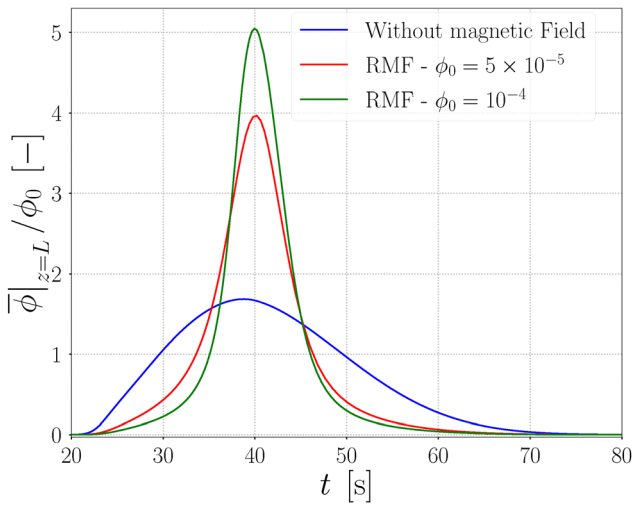

Fig. 12 Effect of injected MNP concentration on outlet signals under an RMF at f_0 = 100 kHz, compared with the no-field case. Parameters: v_0 = 0.25 mm s^{-1} (Pe ≈ 1145, Re ≈ 0.05); H_0 = 14.713 kA m^{-1} (α = 1); injected concentrations $\phi_0 = 5 \times 10^{-5}$ and other values as indicated; particle diameter D_p = 10 nm; domain magnetization M_d = 425 kA m^{-1}.

peak amplitude is higher, than for $\phi_0 = 5 \times 10^{-5}$. This reflects the RMF's more effective suppression of transverse concentration gradients. This behavior is consistent with the idea that increasing particle concentration strengthens the magnetic torque, thereby intensifying the spin-up flow. A stronger spin-up flow enhances transverse mixing, explaining the observed improvement in plug compaction.

Fig. 13 presents the outlet concentration signal, averaged over the cross-section, for $\phi_0 = 5 \times 10^{-5}$ under RMF at different excitation frequencies. Increasing f_0 leads to a reduction in signal variance and an increase in peak amplitude, indicating that the MNP pulse exits the tube in a shorter time with reduced dispersion. This compaction is attributable to the stronger spin-up flow generated at higher frequencies. The increase in f_0 enhances the magnetic torque acting on the fluid, which intensifies the secondary vortex and accelerates the breakdown of transverse concentration gradients.[33–35,42] As a result, axial dispersion is limited and the concentration profile remains sharper, allowing the plug to retain its compact structure over the transport distance.

Although the model includes a macroscopic energy balance (eqn (24)) with a magnetocaloric source term, no measurable magnetocaloric effect was observed in our study, even at the highest excitation frequency of 500 kHz. This absence can be explained by several factors. First, the suspension is highly dilute, so there are insufficient MNPs in the flow to generate significant heating. Second, the microcapillary used here has a small internal diameter (100 μm), which limits the volume occupied by the MNPs and reduces the possibility of heat accumulation. In contrast, Larbi *et al.*[49] reported observable magnetocaloric effects in tubes with hydraulic diameters around 1 mm that were fully filled with concentrated MNP

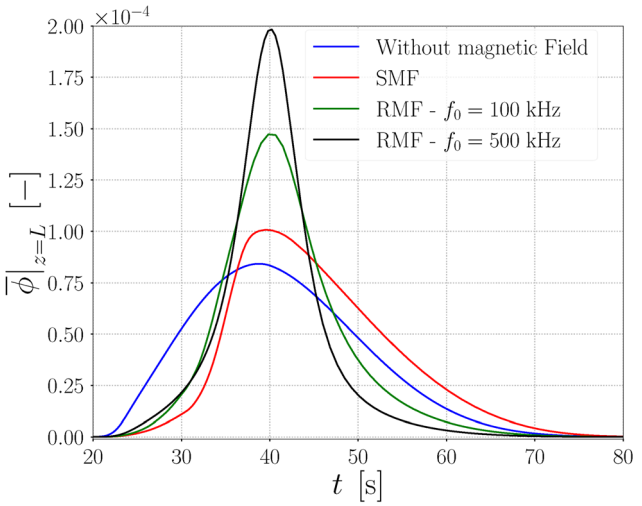

Fig. 13 Effect of RMF frequency on outlet MNP concentration signals for $\phi_0 = 5 \times 10^{-5}$. Parameters: v_0 = 0.25 mm s^{-1} (Pe ≈ 1145, Re ≈ 0.05); H_0 = 14.713 kA m^{-1} (α = 1); particle diameter D_p = 10 nm; domain magnetization M_d = 425 kA m^{-1}.

suspensions. This explains why this effect was observed in their study. In addition, the hydrodynamic configuration plays a major role. In the work of Larbi *et al.*,[49] the magnetocaloric response was examined under a pure spin-up flow generated by an RMF, without any imposed pressure-driven motion. Under such conditions, the fluid elements experience a sustained magnetic torque and longer residence times, favoring local heating. In the present study, the MNP pulse is transported by a pressure-driven Poiseuille flow, which greatly reduces its residence time in the RMF zone and minimizes any potential magnetocaloric contribution.

3.3 Transport of simultaneously injected passive scalar and MNP pulse

To distinguish the contribution of magnetic field–particle interactions from that of purely hydrodynamic dispersion, we consider the simultaneous injection of two pulses into the carrier flow: one containing a passive scalar, the other MNPs. The passive scalar, influenced solely by advection and molecular diffusion, serves as a benchmark for classical laminar dispersion, while the MNPs experience additional magnetic forces. This configuration enables us to assess whether MNPs can act as micro-mixers for the scalar *via* the mechanisms identified in Sections 3.1 and 3.2, namely: (i) secondary flows generated by the KBF under an SMF, (ii) spin-up flows induced by an RMF, and (iii) axial pressure gradients along the plug head caused by transverse KBF-driven flows. The MNPs considered are the same as in the previous sections, with a particle diameter D_p = 10 nm, a magnetic moment M_d = 425 kA m^{-1}, and a Brownian diffusion coefficient $\mathscr{D} = \dfrac{K_B T}{6\mu\pi R_p} = 4.37 \times 10^{-11}$ m^2 s^{-1}. The passive scalar has a molecular diffusion coefficient $D_s = 10^{-9}$ m^2 s^{-1}. The magnetic field amplitude is set to H_0 = 14.713 kA m^{-1}, corresponding to a Langevin parameter α = 1. The injected MNP concentration is varied to examine its impact on scalar transport. Only RMF cases are considered, since we have shown in Section 3.2 that RMF can reproduce the KBF-driven effects observed under SMF.

Fig. 14 compares the transport of simultaneously injected pulses of MNPs and passive scalar at $\phi_0 = 5 \times 10^{-4}$, under an RMF of frequency f_0 = 500 kHz and a space time $\bar{t}$ = 4 s. Panels (a) and (c) show the evolution of the concentration contours in the absence of the RMF, while panels (b) and (d) display the corresponding distributions under the applied RMF. In the absence of the RMF, Fig. 14a and c, both the MNPs and the passive scalar undergo elongation along the streamwise direction due to the parabolic Poiseuille flow. This effect is more pronounced for the MNPs, which exhibit a visibly stronger stretching than the passive scalar. The difference stems from their respective Péclet numbers: $Pe_{MNP} = 1.1 \times 10^4$, nearly twenty times larger than that of the scalar (Pe_s = 500), due to the much smaller Brownian diffusion coefficient of the MNPs.

When the RMF is applied, Fig. 14b and d, the concentration fields display a markedly different behavior. In the case of MNPs, Fig. 14b, oscillatory patterns emerge within the core of the plug transported along the central, high-velocity region of the Poiseuille profile. These fluctuations resemble turbulence-like structures, yet they arise in a purely Stokesian regime where both the Poiseuille flow and the RMF-induced secondary flows (*via* the Kelvin body force and spin-up mechanism) remain fully deterministic. A similar behavior is also observed for the passive scalar, Fig. 14d, confirming that the effect originates from the hydrodynamic perturbations induced by the RMF, rather than from direct magnetic interactions. An additional feature appears at the front of both the MNP and scalar plugs under RMF: a fraction of the concentration field detaches from the leading edge of the main plug. Since this occurs for the passive scalar as well, it must be attributed to transverse pressure gradients and secondary flows induced by the RMF. Similar non-turbulent perturbations of the flow field have been reported in microfluidic systems subjected to other body forces, such as electroosmotic.[38] However, to the best of our knowledge, the detachment of the plug front reported here has not previously been described in such contexts. Furthermore, as inertial terms were neglected in the Navier–Stokes formulation (Stokes flow regime), the observed detachment and oscillations cannot be attributed to inertia-driven instabilities, but rather to body-force-induced secondary flows.

From a mixing perspective, Fig. 14 also highlights a reduction in plug length for both species in the presence of the RMF compared to the no-field case. This contraction indicates enhanced mixing efficiency, demonstrating that MNP pulses subjected to RMF can act as effective micro-mixers for passive tracers. Compared to passive mixing approaches based on microstructures or geometric modulations, our strategy exhibits specific features. While such passive devices indeed enhance mixing,[22] to the best of our knowledge, the front detachment and spatial oscillations observed here have not been reported in that context. Moreover, the pulsed MNP–RMF approach does not require any permanent modification of the channel geometry,

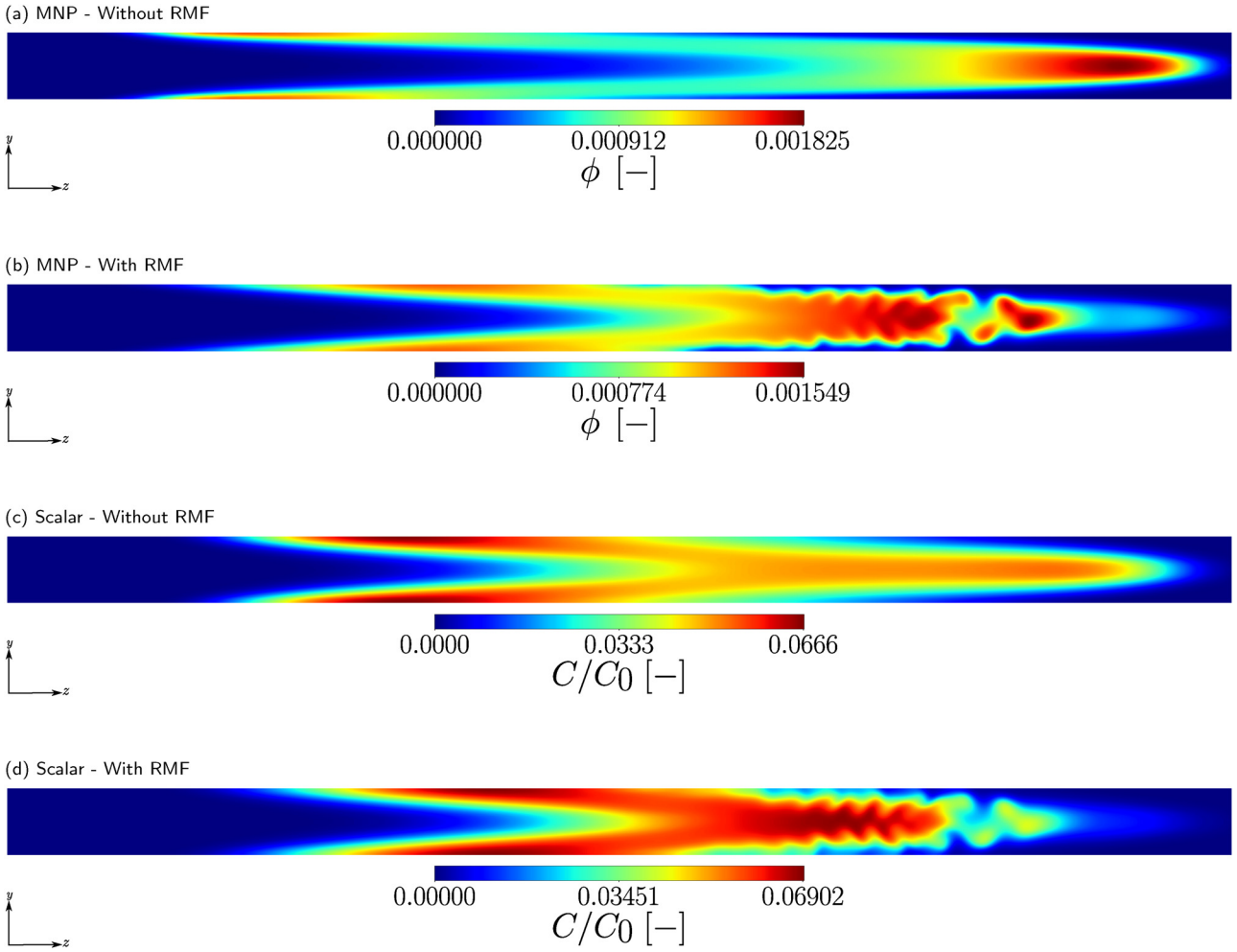

Fig. 14 Comparison of passive scalar and MNP concentration contours at t = 2 s for simultaneous pulse injection with $\phi_0 = 5 \times 10^{-4}$, f_0 = 500 kHz, and space time $\bar{t}$ = 4 s: (a) and (c) without RMF, (b) and (d) with RMF. Parameters: v_0 = 0.25 mm s^{-1} (Pe ≈ 1145, Re ≈ 0.05); H_0 = 14.713 kA m^{-1} (α = 1); particle diameter D_p = 10 nm; domain magnetization M_d = 425 kA m^{-1}.

which is a practical advantage. Like passive mixers, it acts by redistributing axial and transverse momentum. However, pulsed injection of MNPs enables momentum redistribution in both directions, unlike continuous injection of MNPs, where the contribution remains confined to the transverse plane.

A natural question arises when comparing the two space times: why do turbulence-like fluctuations appear at $\bar{t}$ = 4 s but not at $\bar{t}$ = 40 s (Sections 3.1 and 3.2)? What mechanism could be responsible for the persistence of oscillations in one case, and for their disappearance in the other? In particular, one may wonder whether this contrast originates from the balance between advection and diffusion, and how this interplay controls the fate of the secondary structures generated by the RMF.

The contrasting behaviors between the case with a residence time of $\bar{t}$ = 40 s and the one shown in Fig. 14 with $\bar{t}$ = 4 s can be explained by the transport conditions. For $\bar{t}$ = 40 s, the Péclet number of the MNPs is about Pe ≈ 1145, whereas for $\bar{t}$ = 4 s it reaches Pe ≈ 1.1×10^4. This means that the transverse concentration gradients are much more intense at short residence times, strongly enhancing the KBF. Furthermore, the injected concentration of MNPs differs: $\phi_0 = 5 \times 10^{-5}$ for the 40 s case, compared with $\phi_0 = 5 \times 10^{-4}$ in Fig. 14. A higher concentration, combined with stronger gradients, amplifies secondary flows. These two factors explain why fluctuations appear in the case of $\bar{t}$ = 4 s, whereas they remain weaker and less visible in the $\bar{t}$ = 40 s case.

To shed more light on these mechanisms, Fig. 15 presents concentration and axial velocity contours at two characteristic times. At t = 0.37 s, Fig. 15a, the plug of MNPs begins to adapt to the parabolic Poiseuille profile: particles accumulate predominantly in the fast central region, leaving behind a residual concentration near the walls. This asymmetric redistribution generates an axial gradient behind the plug, resulting in a non-uniform transverse distribution. The outcome is an axial pressure gradient, manifested by a slight deformation of the plug head. Such deformation arises because the imbalance between axial and transverse concentration gradients must be compensated by the KBF, which acts to restore equilibrium. However, this deformation is irregular and asymmetric. The reason is that, in addition to the KBF, the system is also influenced by the

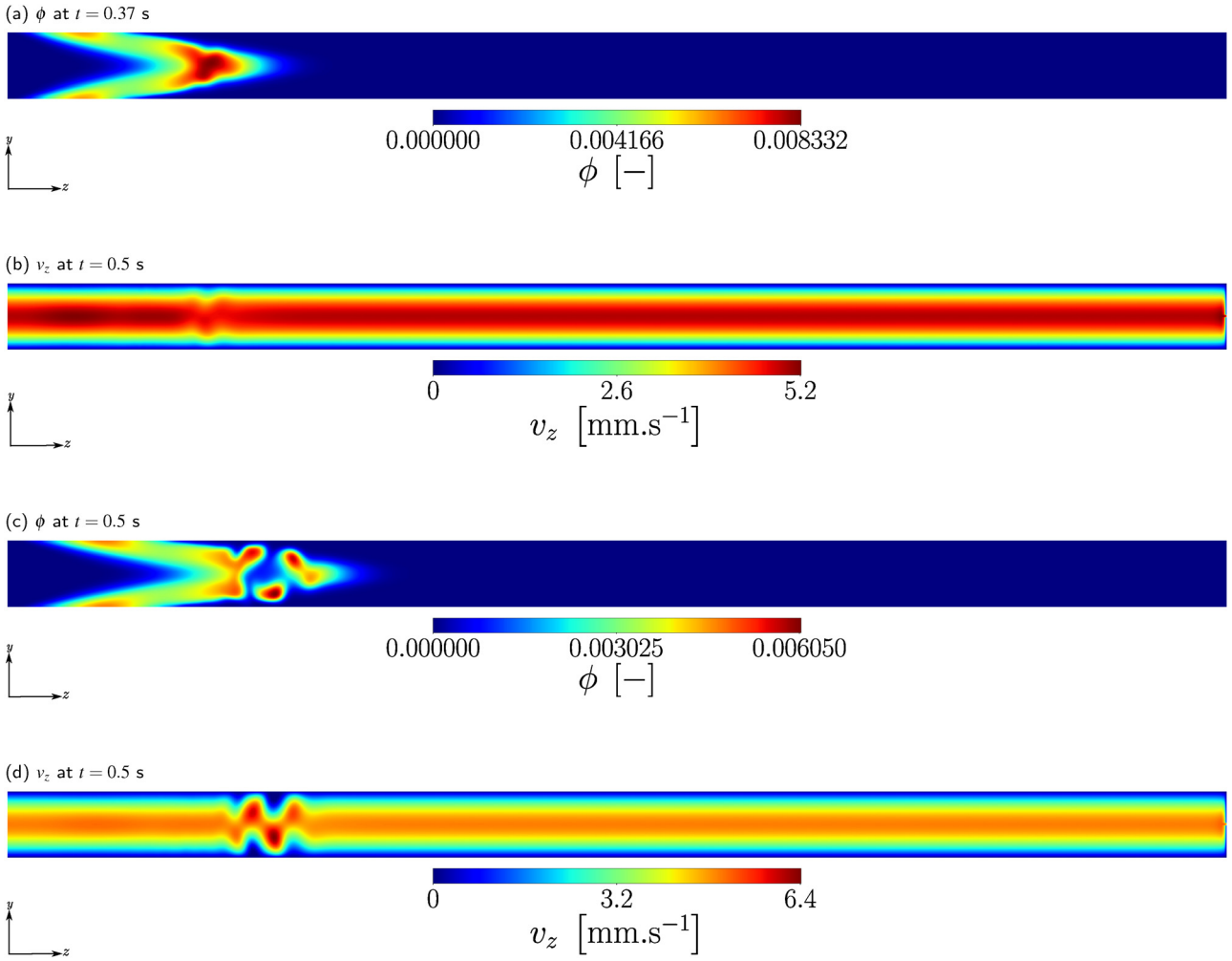

Fig. 15 Contours of MNP concentration (a) and (c) and axial velocity (b) and (d) at t = 0.37 s and t = 0.5 s for $\bar{t}$ = 4 s, Pe ≈ 1.1 × 10^4, and ϕ_0 = 5 × 10^{-4}. Parameters: v_0 = 0.25 mm s^{-1} (Re ≈ 0.05); H_0 = 14.713 kA m^{-1} (α = 1); particle diameter D_p = 10 nm; domain magnetization M_d = 425 kA m^{-1}.

spin-up flow induced by the RMF. This flow transports the MNPs helically, forcing the plug to conform to a spiral-like trajectory. Consequently, the axial pressure gradients at the plug head must follow this dynamic. Consequently, the axial velocity field at t = 0.37 s, exhibits significant spatial oscillations that are essential for understanding this deformation (Fig. 15b).

With time, these oscillations intensify. At t = 0.5 s, Fig. 15c and d, they become strong enough to initiate the detachment of the plug head. The axial velocity field exhibits marked spatial oscillations, which make the head swing from side to side until it progressively separates from the rest of the plug. Upstream of the head, weaker oscillations are also visible, but they remain too small to cause detachment due to lower local MNP concentration and weaker gradients. It is worth noting that in Section 3.2, similar oscillations of the plug head were reported under RMF, but because both the Péclet number and the MNP concentration were lower, they were insufficient to cause detachment.

Finally, the passive scalar behaves like a tracer: it simply follows the secondary flows generated by the MNP plug under the RMF. This indicates that the plug itself can act as a micromixer, transferring its fluctuations to the scalar and thereby enhancing transverse transport.

We now analyze the impact of MNP concentration, residence time $\bar{t}$, and RMF frequency on the simultaneous transport of MNPs and the passive scalar, based on the outlet concentration signals shown in Fig. 16. In the absence of the RMF, Fig. 16a shows that the concentration signal rises very quickly and reaches its maximum at around $t \approx 2.5$ s, much earlier than the imposed residence time of 4 s. This behavior is a direct consequence of the very high Péclet number (Pe ≈ 1.1 × 10^4), which causes the MNP plug located in the fast central streamlines to be convected rapidly toward the outlet. Diffusion is too weak to redistribute the plug across the channel width. After the peak, the signal decays slowly due to the remaining MNPs transported near the wall in the slower regions, which is consistent with classical Taylor dispersion: a sharp front carried by the core and a long tail controlled by wall effects.[53] When the RMF is activated (f = 500 kHz), the outlet signals in Fig. 16a for both concentrations exhibit a clear delay of the

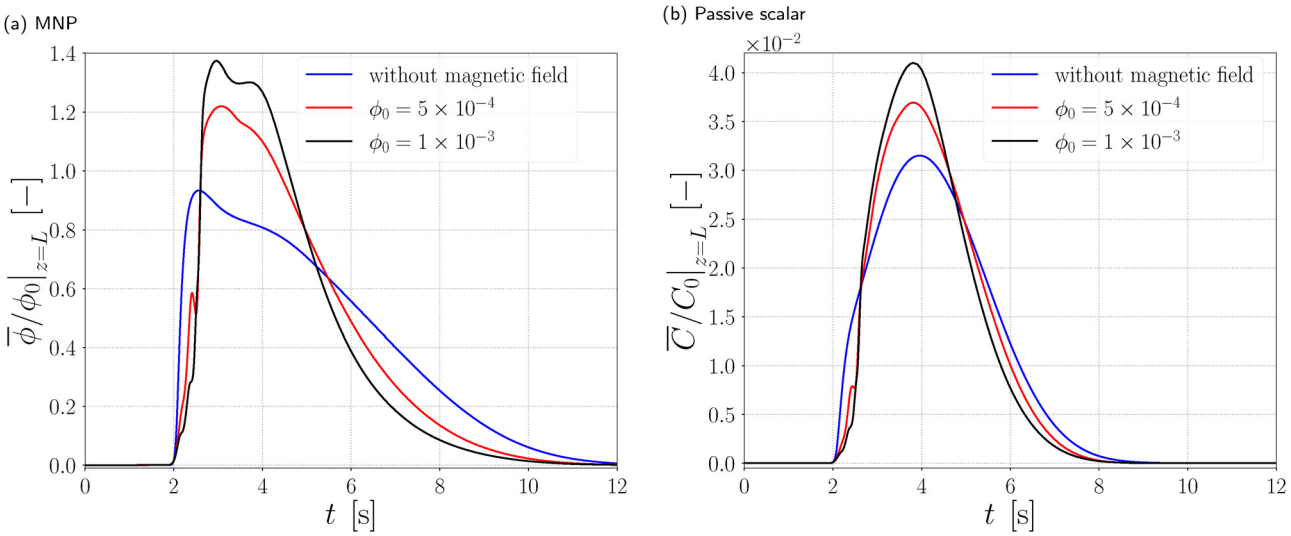

Fig. 16 Outlet concentration signals of MNPs and passive scalar under RMF at f_0 = 500 kHz ($\bar{t}$ = 4 s, Pe_{MNP} = 1.1 × 10^4, Pe_{scalar} = 500): (a) MNPs and (b) passive scalar. Two injected MNP concentrations (5 × 10^{-4} and 10^{-3}) are compared, with the reference case without field shown for comparison. Parameters: v_0 = 0.25 mm s^{-1} (Re ≈ 0.05); H_0 = 14.713 kA m^{-1} (α = 1); particle diameter D_p = 10 nm; domain magnetization M_d = 425 kA m^{-1}.

concentration peak compared to the no-field case. This delay reflects the action of secondary flows (KBF and spin-up flow) opposing the purely convective transport, effectively slowing down the dispersion. At the lower concentration (ϕ_0 = 5 × 10^{-4}), oscillations appear in the signal. For instance, at $t \approx 2.5$ s the concentration briefly decreases before rising again. These oscillations directly echo the deformation and partial detachment of the plug head already observed in Fig. 14. Thus, the fluctuations seen in the outlet signals of Fig. 16a are the macroscopic manifestation of the unsteady plug dynamics driven by the competition between advection, concentration gradients, and RMF-induced transverse flows.

Increasing the MNP concentration enhances these effects. As shown in Fig. 16a, at 10^{-3} the variance of the concentration signal is clearly reduced compared to at 5 × 10^{-4}. This reduction is explained by stronger secondary flows, since both the magnitude of the concentration gradients and the absolute MNP concentration are higher. These conditions amplify the Kelvin body force and spin-up flow, which promote transverse transport and homogenization, thereby narrowing the distribution.

The passive scalar, which has a lower Péclet number (500), behaves differently. As shown in Fig. 16b, the scalar follows the trend of the MNP impulse because it is entrained by the secondary flows induced by the RMF and by the motion of the MNP plug. In both concentrations, the scalar signal shows a reduced variance and a sharper peak compared to the no-field case, a clear indication of mixing. Although the imposed hydrodynamic conditions (large Pe_{MNP}, short residence time) inherently limit mixing, the fact that a measurable reduction of scalar variance is still achieved even at a space time as short as 4 s highlights the strong impact of the magnetocolloidal impulse. This confirms its potential to act as an active agent for controlling scalar dispersion in microchannels.

It should be noted that the classical Taylor–Aris dispersion framework strictly relies on a linear relationship where the inlet concentration affects the output signal proportionally. In our case, MNP transport is inherently nonlinear, as concentration, magnetic field strength, and frequency all feed back into the flow through Kelvin body forces and torque-induced spin-up effects. This explains why an effective dispersion coefficient of Taylor–Aris type cannot be defined here. The oscillatory concentration signals observed in Fig. 16 provide further evidence of this departure from linear Taylor-like dispersion.

We now analyze the case of a longer residence time, $\bar{t}$ = 16 s, shown in Fig. 17. This corresponds to Péclet numbers reduced by a factor of four compared to Fig. 16: for the MNPs ≈ 2.6 × 10^3, and for the passive scalar ≈ 125. Under such conditions, weaker signal distortion is expected in the absence of the RMF, since diffusion becomes more effective in counteracting convective spreading.

Fig. 17a shows the outlet concentration signals of MNPs for both injected concentrations (5 × 10^{-4} and 10^{-3}). In the no-field case, as anticipated, the distortion is less pronounced than in Fig. 16 because the reduced flow velocity decreases the convective bias of the central streamlines, allowing diffusion to partially redistribute the plug. When the RMF is activated at f_0 = 500 kHz, a significant reduction of the variance is observed. This indicates that secondary flows—Kelvin body force and spin-up flow—efficiently suppress radial concentration gradients. These flows have more time to act due to the longer residence time, resulting in stronger homogenization compared to the t = 4 s case. Importantly, no oscillations appear in the signals at $\bar{t}$ = 16 s, since the weaker concentration gradients generated by dispersion are insufficient to trigger the detachment phenomena previously observed in Fig. 16. Increasing the MNP concentration amplifies this effect, as stronger secondary flows further reduce dispersion.

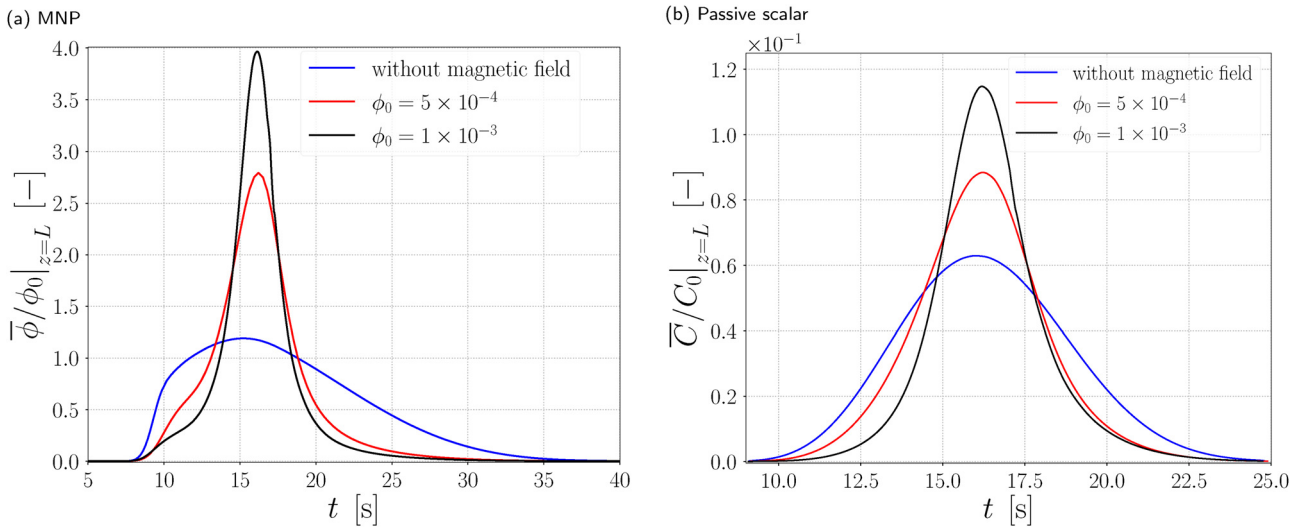

Fig. 17 Outlet concentration signal at $\bar{t}$ = 16 s for $\phi_0 = 5 \times 10^{-4}$ under an RMF at f_0 = 500 kHz: (a) MNPs and (b) passive scalar. Parameters: v_0 = 0.25 mm s^{-1} (Pe ≈ 1145, Re ≈ 0.05); H_0 = 14.713 kA m^{-1} (α = 1); particle diameter D_p = 10 nm; domain magnetization M_d = 425 kA m^{-1}.

The passive scalar signals, reported in Fig. 17b, follow the same trend. A marked reduction in dispersion length is evidenced by the narrower distribution and decreased variance, demonstrating that the scalar benefits from the transverse mixing induced by the MNP impulse. Even though scalar transport occurs at a much lower Péclet number (≈125), the RMF-driven secondary flows further enhance homogenization beyond pure diffusion. This result confirms that magneto-colloidal impulses remain efficient mixers.

Fig. 18 shows the influence of the RMF frequency on the outlet concentration signals for $\phi_0 = 5 \times 10^{-4}$ and a space time of 16 s. Three frequencies were considered: f_0 = 100 kHz, 500 kHz, and 1 MHz. As expected, increasing the frequency from 100 kHz to 500 kHz decreases the variance of both MNP and scalar concentration signals, indicating enhanced mixing. However, at 1 MHz, the variance becomes higher than at 500 kHz, while the concentration peak is reduced, revealing less efficient mixing. This behavior is governed by the dynamics of the spin-up flow, which depend on two characteristic times: the excitation pulsation $\omega_0 = 2\pi f_0$ and the Brownian relaxation time τ_B of the particles. The system behaves analogously to a damped mass–spring oscillator under harmonic forcing: the amplitude increases with frequency until it reaches a maximum when $\omega_0\tau_B \approx 1$, and then decreases once the system can no longer keep pace with the imposed oscillations. Accordingly, at 100 kHz ($\omega_0\tau_B \approx 0.2$), the spin-up flow velocity still increases with frequency. At 500 kHz ($\omega_0\tau_B \approx 1$), it reaches a maximum, resulting in stronger mixing. Beyond this point, at 1 MHz

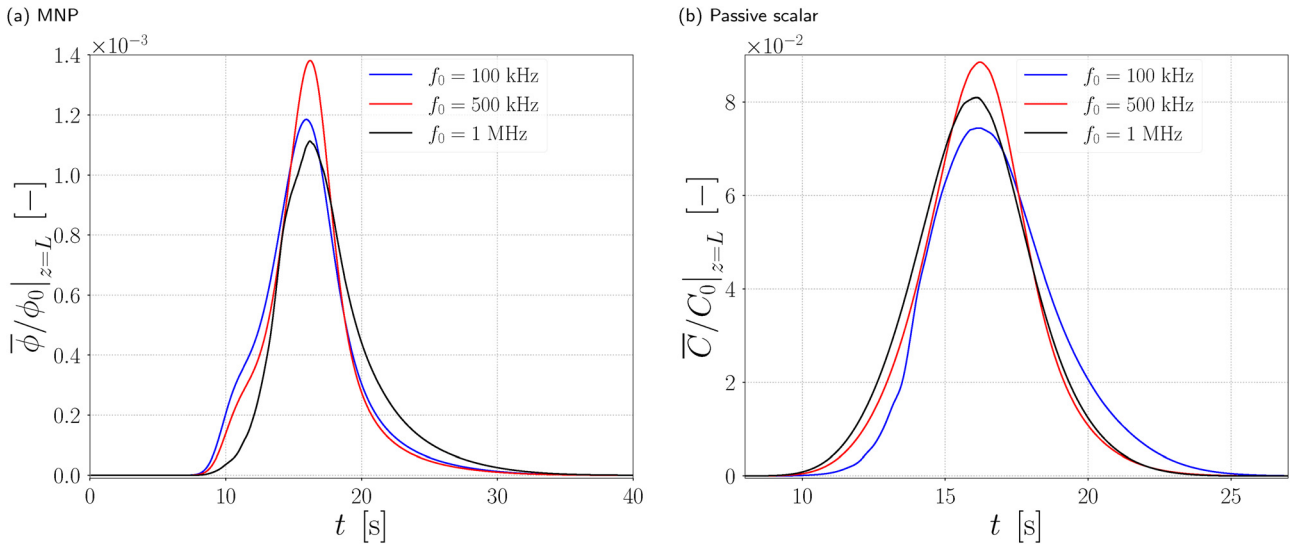

Fig. 18 RMF frequency dependence of outlet concentration signals at $\bar{t}$ = 16 s for $\phi_0 = 5 \times 10^{-4}$: (a) MNPs and (b) passive scalar, showing resonance-like enhancement of mixing at f_0 = 500 kHz. Parameters: v_0 = 0.25 mm s^{-1} (Pe ≈ 1145, Re ≈ 0.05); H_0 = 14.713 kA m^{-1} (α = 1); particle diameter D_p = 10 nm; domain magnetization M_d = 425 kA m^{-1}.

($\omega_0\tau_B \approx 2$), the system response declines, explaining the reduced mixing observed. This resonance-like mechanism linking the external frequency and the Brownian characteristic time has been recently documented in the literature.[42]

These frequency-dependent results should be interpreted within the broader parameter space of the model. In the present study, we restricted the analysis to $\alpha \leq 1$ and particle concentrations below 1%, since clustering occurs beyond these limits and the Smoluchowski and Faxén formalisms no longer apply. The case corresponding to $\alpha = 1$ (*i.e.*, the field amplitude $H_0 = 14.713$ kA m^{-1} chosen here) represents the strongest expected effect within the single-particle regime, while the influence of concentration, field intensity, and RMF frequency has already been systematically established and experimentally validated in our previous studies.[33–35,42,49]

The present model cannot be directly validated in the pulse configuration considered here, since no experimental data exist for magnetically driven MNP pulses. Nevertheless, the underlying transport framework, which couples MNP dynamics with momentum exchange in the carrier flow, has already been developed and validated in different contexts: spin-up flows under RMF were shown to agree with velocity field measurements by Torres-Diaz *et al.*,[36] passive scalar dispersion was validated against the experiments of Boroun and Larachi[31] and the classical Taylor dispersion benchmark, and high-frequency RMF dynamics were corroborated with magnetic torque measurements from Torres-Díaz *et al.* (2014). The present contribution therefore extends a validated theoretical framework into the new regime of pulsed MNP injection under SMF and RMF, for which, to the best of our knowledge, no experimental studies are currently available.

The present pulse configuration cannot be directly validated, as no experimental data exist for magnetically driven MNP pulses. Nevertheless, the underlying transport framework (MNP dynamics coupled to momentum exchange in the carrier flow) has been validated in related settings: (i) Larbi *et al.*[35] validated the model's RMF spin-up predictions against the local velocity field measurements of Torres-Diaz *et al.*;[36] (ii) Larbi *et al.*[33] validated the model in the context of passive scalar dispersion, showing that it reproduces the classical Taylor dispersion benchmark and matches passive-scalar breakthrough curves reported experimentally by Boroun and Larachi;[31] (iii) Larbi *et al.*[42] validated the high-frequency RMF regime by comparing the model's magnetic-torque predictions with the torque measurements of Torres-Diaz *et al.*[36] The present contribution therefore extends a previously validated theoretical framework into the new regime of pulsed MNP injection under SMF and RMF, for which, to the best of our knowledge, no experimental studies are currently available.

It should be noted that global indicators, such as dispersion coefficients and mixing indices, are often used in classical transport studies but are not well suited to this problem. The nonlinear nature of MNP transport—arising from the coupling of concentration, magnetic field strength, frequency, and Kelvin body forces and torque—precludes the use of a single effective dispersion coefficient of the Taylor–Aris type. Furthermore, mixing indices are usually defined in reactive systems to help interpret conversion rates,[28] which is not applicable here. Taking such a statistical approach would require a separate investigation and would stray from the central focus of this work: identifying and characterizing the mechanisms that drive dispersion under pulsed MNP injection. For this reason, we focused on complementary diagnostics, such as breakthrough curves, velocity fields, and concentration contours, which provide direct physical insight into how magnetic forcing reshapes dispersion.

4 Conclusions

This study examined the transient dynamics of magnetically responsive nanoparticle pulses injected into a Taylor microcapillary flow and their influence on dispersion under SMF and RMF. By contrasting these two configurations, we identified the distinct mechanisms that govern flow modification and mixing. Under SMF, the KBF arises from concentration gradients induced by Poiseuille flow, producing transverse motion that compacts the pulse and reduces radial concentration gradients, while axial non-uniformity drives localized pressure variations at the pulse head. These hydrodynamic signatures dissipate as the pulse passes, highlighting the transient nature of SMF-induced effects.

Under RMF, the KBF couples with a spin-up flow generated by magnetic torque, leading to more complex and sustained behavior. The spin-up mechanism dominates cross-stream transport, reducing variance and maintaining transverse homogenization, while axial KBF effects persist. At short residence times and high nanoparticle Péclet numbers, the combined action of KBF and spin-up induces oscillations and partial front detachment, features reminiscent of turbulence-like dynamics in otherwise laminar conditions. For longer residence times, diffusion progressively smooths these structures, but the spin-up continues to enhance mixing efficiency. A key outcome is the identification of a Péclet-number criterion linking MNP transport to scalar entrainment: because MNPs are much less affected by diffusion than the passive scalar, they generate secondary hydrodynamic structures that entrain and redistribute the scalar field.

Overall, the findings show that the "MNP pulse + RMF" strategy not only reproduces the beneficial KBF effects observed under SMF but also adds a strong rotational component that intensifies mixing, enables transient front detachment, and maintains redistribution even at long residence times. This dual mechanism positions MNP pulses under RMF as a versatile and effective strategy for active control of Taylor dispersion in microchannels, with potential applications in microreactor design and lab-on-a-chip platforms.

Author contributions

Zakaria Larbi: conceptualization, investigation, formal analysis, validation, writing – original draft; Faïçal Larachi: conceptualization,

formal analysis, writing – review & editing; Seyed Mohammad Taghavi: writing – review & editing; Abdelwahid Azzi: writing – review & editing.

Conflicts of interest

The authors report no conflicts of interest.

Data availability

All figures supporting the findings of this study have been deposited in Figshare and are openly available at **https://doi.org/10.6084/m9.figshare.29983432**.

Acknowledgements

The authors thank the Natural Sciences and Engineering Research Council of Canada for its financial support *via* FL discovery grant.

Notes and references

1 D. Li, Y. Zhao, Z. Nie, J. Tang, R. Wang, J. Lu, Y. Xing and F. Yu, *Chem. Commun.*, 2025, **241**, 14022–14038.
2 J. Wang, J. E. Butler and A. J. Ladd, *Proc. Natl. Acad. Sci. U. S. A.*, 2025, **122**, e2417757122.
3 C. L. Lambert, G. van Mierlo, J. J. Bues, O. J. Guillaume-Gentil and B. Deplancke, *Nat. Genet.*, 2025, 1–13.
4 F. Enzmann, M. Stöckl, A.-P. Zeng and D. Holtmann, *Eng. Life Sci.*, 2019, **19**, 121–132.
5 S. Shamsian, A. B. Siddique, V. Kordzadeh-Kermani, L. de la Vega Tejuca, F. Falcone, M. Ray, S. N. Ashrafizadeh, S. O. M. Chapa, M. J. Madou and M. Madadelahi, *Microsyst. Nanoeng.*, 2025, **11**, 127.
6 A. Ratanpara, Y. Li and M. Kim, *Lab Chip*, 2025, DOI: **10.1039/D5LC00208G**.
7 K. Gomez, V. R. Yarmey, H. Mane and A. San-Miguel, *Annu. Rev. Chem. Biomol. Eng.*, 2025, **16**, 195–216.
8 P. Dehghani, A. Sinquin, N. Gland, E. Lécolier, L. Ruffine and A. M. Tang, *Lab Chip*, 2025, **25**, 2903–2917.
9 J. Song, S. Meng, J. Liu and N. Chen, *Biomicrofluidics*, 2025, **19**, 011501.
10 S. Gimondi, H. Ferreira, R. L. Reis and N. M. Neves, *ACS Nano*, 2023, **17**, 14205–14228.
11 V. Sharma, J.-U. Joo, A. Mottafegh and D.-P. Kim, *Chem. Eng. J.*, 2025, 164284.
12 M. M. Saeed, E. Carthy, N. Dunne and D. Kinahan, *Lab Chip*, 2025, **25**, 3060–3093.
13 E. Khanjani, A. Fergola, J. A. López Martnez, S. Nazarnezhad, J. Casals Terre, S. L. Marasso and B. Aghajanloo, *Front. Lab Chip Technol.*, 2025, **4**, 1502127.
14 S. S. Mabaleha, A. Sandaruwani, C. Peng, D. Zou, W. Ren, C.-X. Zhao and X. Xu, *Mater. Sci. Eng., R*, 2025, **165**, 101005.
15 K. Fibben, E. K. Williams, J. D. Roback, W. A. Lam and D. N. Alter, *Lab Chip*, 2025, **25**, 2566–2577.
16 S. Izaddoust, I. Poves-Ruiz, E. A. Hualde, D. Patko, L. Florea, C. Delaney, L. Basabe-Desmonts and F. Benito-Lopez, *Lab Chip*, 2025, DOI: **10.1039/D5LC00259A**.
17 Q. Ruan, W. Guo, R. Yang, T. Sun, Q. Yang and Y. Ren, *Biomaterials*, 2025, 123617.
18 Y. Xu, M. T. J. Chan, M. Yang, H. Meng and C.-H. Chen, *Lab Chip*, 2025, **25**, 1282–1295.
19 I. Kundacina, O. Kundacina, D. Miskovic and V. Radonic, *Lab Chip*, 2025, **25**, 657–672.
20 J.-C. Hsu and K.-L. Liao, *Sens. Actuators, A*, 2025, 116600.
21 L. Cocconi, Y. Shi and A. Vilfan, *Phys. Rev. Lett.*, 2025, **135**, 037101.
22 E. Bennour, N. Kaid and A. Mouissi, *Ind. Eng. Chem. Res.*, 2024, **63**, 2861–2874.
23 S. F. Javed, M. E. Khan, Z. Yahya, M. J. Idrisi and W. Tenna, *Sci. Rep.*, 2025, **15**, 18140.
24 D. Kumar, S. K. Mehta and P. K. Mondal, *Langmuir*, 2025, **41**, 7624–7639.
25 S. K. Mehta and P. K. Mondal, *Phys. Rev. Fluids*, 2024, **9**, 023301.
26 P. Hajiani and F. Larachi, *Chem. Eng. J.*, 2012, **203**, 492–498.
27 P. Hajiani and F. Larachi, *Chem. Eng. J.*, 2013, **223**, 454–466.
28 S. Boroun and F. Larachi, *AIChE J.*, 2017, **63**, 337–346.
29 S. Boroun and F. Larachi, *Curr. Opin. Chem. Eng.*, 2016, **13**, 91–99.
30 S. Boroun and F. Larachi, *Chem. Eng. J.*, 2020, **380**, 122504.
31 S. Boroun and F. Larachi, *Chem. Eng. Sci.*, 2020, **224**, 115770.
32 R. E. Rosensweig, *Ferrohydrodynamics*, Courier Corporation, 2013.
33 Z. Larbi, F. Larachi and A. Azzi, *Chem. Eng. J.*, 2024, **493**, 152528.
34 Z. Larbi, F. Larachi and A. Azzi, *Chem. Eng. Sci.*, 2025, **310**, 121547.
35 Z. Larbi, F. Larachi and A. Azzi, *J. Fluid Mech.*, 2024, **980**, A37.
36 I. Torres-Diaz, A. Cortes, Y. Cedeño-Mattei, O. Perales-Perez and C. Rinaldi, *Phys. Fluids*, 2014, **26**, 012004.
37 G. I. Taylor, *Proc. R. Soc. London, Ser. A*, 1953, **219**, 186–203.
38 C. J. Samuel, R. Chang, K. Ma and J. G. Santiago, *J. Fluid Mech.*, 2025, **1011**, A36.
39 A. Alexandre, T. Guérin and D. S. Dean, *Phys. Rev. E*, 2025, **111**, 064124.
40 D. Saintillan and M. J. Shelley, *Complex fluids in biological systems: Experiment, theory, and computation*, Springer, 2014, pp. 319–355.
41 B. Ezhilan and D. Saintillan, *J. Fluid Mech.*, 2015, **777**, 482–522.
42 Z. Larbi, F. Larachi, S.-M. Taghavi and A. Azzi, *Phys. Fluids*, 2025, **37**, 072040.
43 E. Furlani and K. Ng, *Phys. Rev. E:Stat., Nonlinear, Soft Matter Phys.*, 2006, **73**, 061919.
44 B. Sobac, Z. Larbi, P. Colinet and B. Haut, *Colloids Surf., A*, 2019, **576**, 110–122.
45 Z. Larbi, N. Sadoun, E.-K. Si-Ahmed and J. Legrand, *Int. J. Heat Mass Transfer*, 2021, **165**, 120613.
46 C. Loussert, A. Bouchaudy and J.-B. Salmon, *Phys. Rev. Fluids*, 2016, **1**, 084201.
47 P. Danckwerts, *Chem. Eng. Sci.*, 1953, **2**, 1–13.

48 O. Levenspiel, *Chemical reaction engineering*, John Wiley & Sons, 1998.
49 Z. Larbi, F. Larachi, S.-M. Taghavi and A. Azzi, *Int. J. Heat Mass Transfer*, 2026, **254**, 127686.
50 D. S. Viswanath, T. K. Ghosh, D. H. Prasad, N. V. Dutt and K. Y. Rani, *Viscosity of liquids: theory, estimation, experiment, and data*, Springer, Dordrecht, The Netherlands, 2007.
51 C. Vázquez-Vázquez, M. López-Quintela, M. Buján-Núñez and J. Rivas, *J. Nanopart. Res.*, 2011, **13**, 1663–1676.
52 R. E. Rosensweig, *J. Magn. Magn. Mater.*, 2002, **252**, 370–374.
53 M. Giona, A. Adrover, S. Cerbelli and F. Garofalo, *Phys. Fluids*, 2009, **21**, 123601.
54 M. Wörner, *Chem. Eng. Sci.*, 2025, 122116.
55 S. S. Leong, Z. Ahmad and J. Lim, *Soft Matter*, 2015, **11**, 6968–6980.
56 I. Raouf, J. Lee, H. S. Kim and M.-H. Kim, *Int. J. Therm. Sci.*, 2021, **159**, 106604.

